Tribology International 204 (2025) 110529

Contents lists available at ScienceDirect

Tribology International

journal homepage: www.elsevier.com/locate/triboint

Bi-directional evolution of graphenic vacancy structure in oxygen plasma treatment

Yinong Chen [a,1], Shuyu Fan [a,1], Shu Xiao [a,*], Hu Zhang [a], Yi Wu [a], Jing Wu [a], Guoliang Tang [a], Fenghua Su [a], Paul K. Chu [b]

[a] School of Mechanical & Automotive Engineering, South China University of Technology, Guangzhou 510641, China
[b] Department of Physics, Department of Materials Science and Engineering, and Department of Biomedical Engineering, City University of Hong Kong, Tat Chee Avenue, Kowloon, Hong Kong

ARTICLE INFO

Keywords:
Graphene
Oxygen plasma
Defect engineering
Molecular simulation

ABSTRACT

The phenomenon of friction increase in graphenic materials during prolonged treatment in an oxygen plasma environment has been widely recognized. In this study, we report a possible oxidation state that leads to decreased friction during oxygen plasma treatment of graphenic materials through molecular simulations. We also propose a simple, clean, and efficient method to control the reverse structural evolution for controlled oxidation. Experimental applications demonstrated a 30.6 % reduction in friction and a 130.1 % increase in friction for short and long oxygen plasma treatments, respectively, compared to the initial graphenic vacancy structure. These findings contribute to an increased understanding of the response and modulation of graphenic coatings in oxygen plasma environments.

1. Introduction

The need for key components in spacecraft to work stably for a long time in the harsh space environment is mandatory. However, frictional wear occurs at the interfaces of all moving parts including spacecraft engines, solar panels, and space grippers, and is the main cause of energy loss and failure of mechanical systems [1,2]. Nearly 60 % of all mechanical system failures are wear-related, and frictional energy consumption accounts for a quarter of global primary energy consumption [3–5]. In the space environment, for example, heavy contact stress (2 GPa and above), high-energy plasma, and high vacuum, the energy loss and equipment failure caused by friction and wear are even more severe. In the case of oxygen plasma, the lubricating interface may be etched and damaged leading to failures. Therefore, to extend the equipment lifetime, save energy, and reduce harmful emissions, it is imperative to study the evolution of lubrication coatings in extreme environments which enables to improvement of the lubrication properties of mechanical components under harsh conditions [4,6,7].

Oxygen plasma, consisting of oxygen particles such as atoms, molecules, ions, and electrons, is prevalent in the space and semiconductor industry. It is produced when energetic and charged particles attack oxygen-containing gases usually in the vicinity of high-energy objects. It is also common on Earth and Mars because the atmospheres are eroded by solar wind [8]. During oxygen plasma bombardment, the friction surfaces may be oxidized and corroded, causing cracks and wear [9–12]. Therefore, stable and etch-resistant lubrication coatings are crucial to mitigate wear failure in the oxygen plasma environment.

Graphenic materials have attracted much attention in this field due to their unique structure and properties. Owing to the atomic lamellar structure [6], large specific surface area [13], excellent thermal stability [14], high intrinsic tensile strength [15], and low interlayer van der Waals barrier [16], graphenic materials possess exceptional antifriction and anti-wear properties, which are superior to those of traditional lubrication materials [17–21]. The stability of graphenic materials gives rise to low atom adsorption and reaction even being bombarded by high-energy oxygen particles. The large carbon-carbon bonding energy makes it difficult to etch atoms from the surface, and graphenic materials are also impassable to most particles and ions (except for protons), consequently producing good lubrication and resistance to etching and deleterious surface reactions [22]. In fact, graphenic materials, in principle, can be a revolutionary lubricating material in space to prevent the undesirable effects produced by oxygen plasma. However, graphenic

* Corresponding author.
E-mail address: xiaos@scut.edu.cn (S. Xiao).
[1] These authors contributed equally to this work.

https://doi.org/10.1016/j.triboint.2025.110529
Received 11 November 2024; Received in revised form 29 December 2024; Accepted 11 January 2025
Available online 13 January 2025

material defects amplify the effects of plasma on coatings. Vacancies [23,24], edges [25], wrinkles [26], and torsion angles [27,28] can alter the properties of graphenic materials and enhance the coupling effects of defective graphenic materials with oxygen plasma. There are two main ways to make graphenic materials etch-resistant and wear-resistant in the harsh space environment. Firstly, improving the structural ordering and coverage of graphenic materials hinders plasma etching, and it can be achieved by improving the CVD or transfer processes [22,29]. However, this method is relatively expensive and impractical. Secondly, defect engineering is an effective means to cope with the coupling effects between defects with oxygen plasma.

Defect engineering of graphenic materials has emerged to be a practical strategy to modulate the material properties, and it has been shown that the friction properties can be enhanced by modification with fluorine, hydrogen, and oxygen [30–34]. In the oxygen plasma environment, graphenic materials exhibit simultaneous adsorption and vacancy expansion. However, the fundamental principles underlying this phenomenon are still not well understood. Gajurel et al. have proposed that wrinkles induced by vacancies are the key factor influencing friction properties, while the influence of surface functional groups is comparatively minor [35]. Yuan et al. have observed that prolonged oxidation of graphenic materials increases interlayer friction due to the additional hydrogen bonds [36]. Other investigations have focused on vertical anisotropic etching and thermal reduction [37,38]. Nonetheless, systematic studies on the relationship between regulations in oxygen plasma experiments and frictional properties of graphenic material coatings are heretofore still limited. In particular, the microstructural evolution from vacancies to oxygen adsorption states, vacancy expansions, and their impact on friction remain unresolved. Hence, a systematic study is crucial to enriching our understanding of the etching resistance and lubricating properties of graphenic materials in the oxygen plasma environment.

Herein, Density Functional Theory (DFT) calculations are used to investigate the changes in friction during the structural evolution and the causes. Molecular dynamics (MD) simulated the friction-induced structural reversal and elucidated its kinetic mechanism. It is found that the friction in the atmosphere also decreases and then increases, while low-load and low-speed friction allows the reverse evolution of structure to a low-friction form, which may also be caused by the change of C-O and C═O quantities. The results reveal the temporal effects of oxygen plasma on the friction properties of graphenic coatings and propose a simple and cost-effective method of inducing structural evolution to form optimal surface structures. The findings could have economic benefits while enhancing our fundamental understanding of the structural evolution of graphenic materials facing complex oxygen plasma environments.

2. Calculations and experimental details

2.1. First-principles calculations

First-principles calculations were performed utilizing the density-functional semi-core pseudopotential approach within the DMol3 software package [39]. The exchange-correlation effects were described using the general gradient approximation (GGA) with the Predew-Burke-Ernzerhof (PBE) functional [40,41], while Grimme's customized method was applied to account for the dispersion interactions [42]. Spin polarization was incorporated into the calculations, and optimization procedures were executed until meeting the convergence criteria for self-consistent field (SCF) tolerance, total energy, atomic forces, and maximum displacement, set at values below 2.7×10^{-5} eV, 2.7×10^{-4} eV/atom, 0.054 eV/Å, and 5×10^{-3} Å (1 Ha ≈ 27.2114 eV), respectively. The calculations were performed using the (2 × 4) cell of the three-layer graphenic model (8.52 Å × 9.84 Å × 23.6 Å) after matrix transformation ($M = \begin{matrix} 2 & 1 \\ 0 & 1 \end{matrix}$). A vacuum layer with a thickness greater than 10 Å was added to avoid the interactions between layers under the periodic boundary condition. A 6 × 6 × 1 k-mesh grid was employed to acquire relatively accurate results. V_n-N indicates the type of structures shown in Fig. 1b, V referring to vacancies, n referring to the number of vacancies, and N referring to the number of adsorbed oxygen atoms. Based on the single carbon vacancy, V_1-0, V_1-1, and V_1-3 structures were established to investigate the surface properties and friction properties. V_2-0, V_2-1, and V_2-4 were built as counterparts for expanded two carbon vacancies. All the constructed structures were stable, as inferred from the negative binding energy (E) in Table S1 in the Supplementary Material.

The adsorption energy (E_{ads}) and etching energy (E_{etch}) were used to characterize the tightness of oxygen atoms or carbon atoms bound to the surface structures. E_{ads} and E_{etch} were respectively calculated by Eq. (1) and Eq. (2):

$$E_{ads} = E_{total} - E_o - E_{substrate}, \tag{1}$$

$$E_{etch} = E_{total} - E_c - E_{substrate}, \tag{2}$$

where E_{total} is the total energy of the graphenic system, E_o and E_c are the energy of isolated oxygen atoms and etched carbon atoms, and $E_{substrate}$ is the energy of the substrate, respectively. The etching energy describes the energy required for the expansion of carbon vacancy defects in graphenic coatings in the oxygen plasma. The layer binding energy (E_b) is used to describe the tightness of the layer combination, and negative values indicate a more stable state. The magnitude of the external force can be measured by fixing the upper friction pair in the z-direction and calculating its binding energy to the surface model at different interfacial distances (refer to Fig. 2). E_b was calculated by Eq. (3):

$$E_b = E_{total} - E_{up} - E_{down}, \tag{3}$$

where E_{up} and E_{down} are the energy of the upper layer of the friction pair and lower graphenic three-layers.

To simulate the load friction in the experiment, we adopt the constant interface model where atoms in friction pairs are constrained relative to each other [43]. It is a common practice to predict applications with constant interface model results [44]. We focus on the friction characteristics at two interface distances with heavy load (2 GPa) and light load (0 GPa). An external force F_{ext} σ_{ext} was calculated as a differential of the binding energy concerning the interlayer distance (*z-direction*, referring to Fig. 2a and Fig. 2c for more information) and calculated interlayer contact stress, as shown in Eqs. (4) and (5):

$$F_{ext} = -\partial E_b(z)/\partial z, \tag{4}$$

$$\sigma_{ext} = F_{ext}/A, \tag{5}$$

In the potential energy surface (PES) calculations [45,46], the potential energy (E_p) was calculated with respect to a reference (E_0) at the prefixed interfacial distance with external force using a constant interface distance model, as shown in Eq. (6):

$$E_p(D, \sigma_{ext}) = E_b(D, z(D, \sigma_{ext})) + F_{ext} \cdot \Delta z(D, \sigma_{ext}) - E_0(D_0, \sigma_{ext}), \tag{6}$$

where D is the distance along the sliding path, and Δz refers to the difference in height of the friction pair relative to the initial position. The first term represents the potential energy under pressure, the second term represents the work against the external force, which does not do work under the constant interfacial distance model. The third term denotes the minimum potential energy on the surface. The theoretical friction force $F_s(D, \sigma_{ext})$ was calculated as the derivative of the potential energy profile along the sliding path [47], as shown in Eq. (7):

$$F_s(D, \sigma_{ext}) = \begin{cases} \dfrac{-\partial E_p(D, \quad \sigma_{ext})}{\partial D}, \& F_s > 0 \\ 0 \quad , \& F_s \le 0 \end{cases}. \tag{7}$$

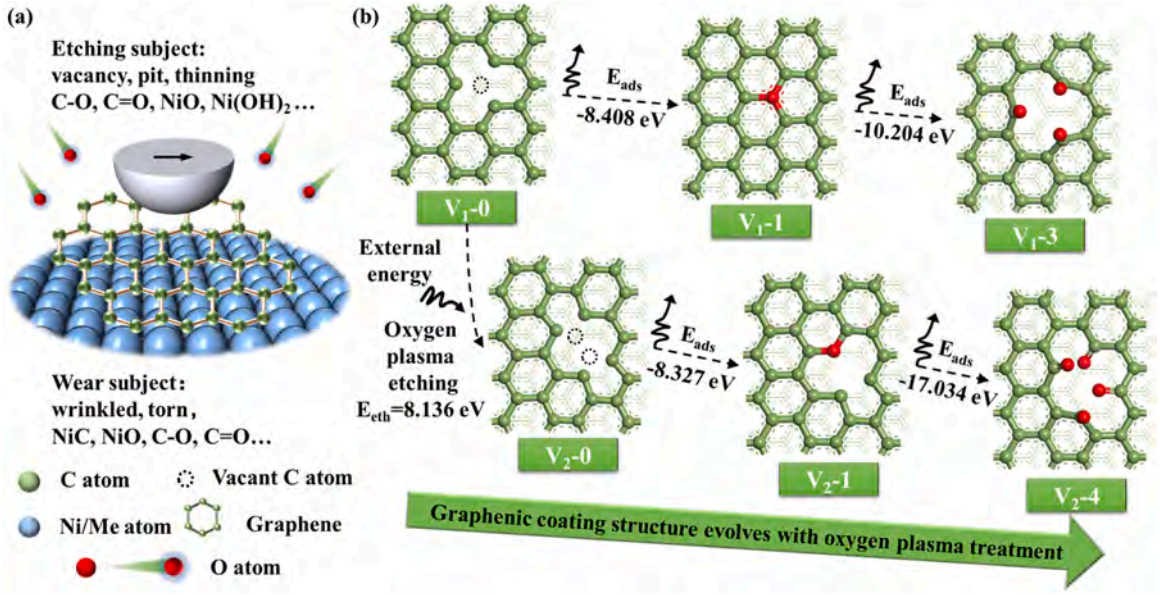

Fig. 1. Evolution of graphenic materials in oxygen plasma: (a) Schematic diagram of etching and wear; (b) Evolution of atomic vacancy defects in graphenic material under oxygen plasma treatment. (V_n-N indicating the type of structures, V referring to vacancies, n referring to the number of vacancies, and N referring to the number of adsorbed oxygen atoms).

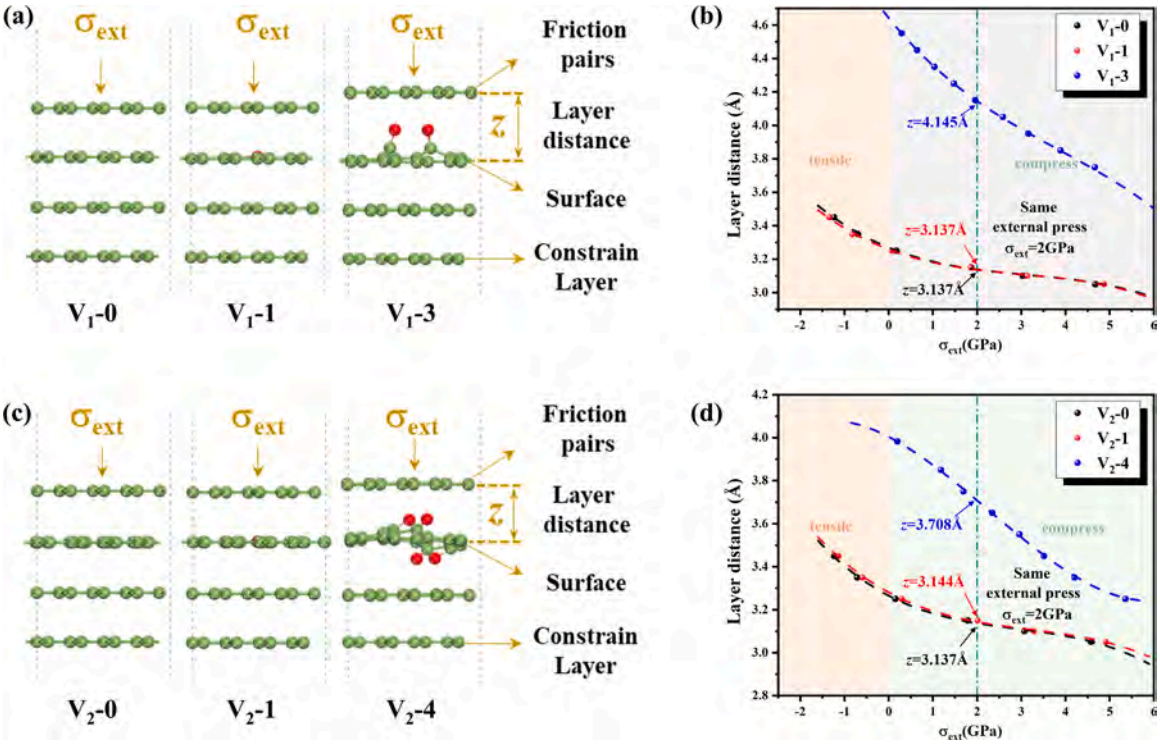

Fig. 2. Constant interface distance modeling and determination of interface spacing from external forces: (a) (c) Side view of the models of the three-layer graphene structure with transferred graphene friction pairs under external layer stress; (b) (d) Layer distances at the same stress of 2 GPa by fitting the data corresponding to layer distance (**z**) and external stress (σ_{ext}). Please refer to Table S3 for the detailed curve fitting information.

It is postulated that any work performed by a negative friction force is absorbed by the phonon energy dissipation mechanism in the friction system. Consequently, Eq. (7) does not account for negative friction forces. To quantitatively compare the friction properties, the average friction force (F) is calculated as the ratio of the difference in potential energy between the highest and lowest points of the path to the distance [48].

The differential electron density, Mulliken population, and partial density of states (PDOS) were derived to elucidate the mechanism for the structural optimization [49]. The Mulliken population analysis, introduced in 1955, serves as a tool for characterizing the charge distribution among atoms [50]. By examining the Mulliken charge and bond population, the bonding interactions between atoms can be quantitatively assessed and compared.

2.2. Molecular dynamics simulation

To analyze the mechanism of friction-induced structural evolution of graphenic oxide materials, we performed molecular dynamics simulations using reactive force fields (ReaxFF) in a software called Large-scale Atomic/Molecular Massively Parallel Simulator (Lammps). The ReaxFF potential function is used to describe interatomic interactions during simulations [51]. Qualitative comparisons between experimental results and ReaxFF molecular dynamics simulations have proven the validity and versatility in the last years [34,52–54]. The ReaxFF potential function is capable of evaluating complex physical and chemical behaviors in interfacial processes [34,52–54]. As a result, ReaxFF potential functions have been used to describe how carbon-oxygen-aluminum atoms interact with each other [51].

The oxide graphenic material was formed by stacking three graphene layers with a size of 102.26 Å along the x-axis and 59.04 Å along the y-axis. As shown in the supplementary material Fig. S4, the leftmost 2 Å of atoms were fixed to ensure that no graphene interlayer sliding phenomenon occurs during the sliding of the alumina ball to the right to focus on the friction-induced evolution of the surface structure. The system was relaxed for 5 ps at 300 k in the NVT regime with a timestep of 0.1 fs, and then the rigid alumina ball was placed 4 Å above the plane of the Newtonian layer of graphene and pressed down to a depth of 4 Å to ensure full contact. The entire friction process takes place in a vacuum environment in the NVE regime. The downward and rightward sliding speeds were both 0.2 Å/ps and the total friction distance was 500 Å. The atomic action of the reactive force field dictates that when oxygen pulls away from neighboring carbon due to friction, impact, warming, etc., there is a possibility of breaking the C/O bond, which enables the desorption of oxygen atoms and induces the formation of oligo-oxygen structures. Aluminum oxide has good etch resistance and is a commonly used material for plasma environment devices. The temperature of the friction process and the coordination of oxygen atoms in the sliding path were recorded to illustrate the friction-induced evolution of the surface oxygen structure.

The constant strain method provided equal strain for a series of steps in all directions to calculate the mechanical properties. The elastic modulus was calculated by applying equal strain to the armchair directions of different oxygen-bonded surfaces. The elastic modulus of perfect graphene calculated by this method was in the normal range of 1.14 TPa [55]. A larger modulus of elasticity means a smaller possibility for wrinkles or breaking during friction, thus maintaining structural stability and reducing the number of interacting atoms, ultimately resulting in durable low friction [56].

2.3. Materials preparation, tribological assessment, and characterization

The graphenic coating was grown by HFCVD (Hot filament chemical vapor deposition) on a WC-Co substrate with a 2 μm nickel (Ni) substrate (Fig. S1 in the Supplementary Material for details). Oxygen plasma treatment was carried out in a PVD unit, and the vacuum chamber was pre-evacuated to 9×10^{-4} Pa before the treatment. Oxidation was carried out at a working air pressure of 0.48 Pa, with an adjusted oxygen flow rate of 30 sccm. Oxygen was dissociated at the anode layer linear ion source at 1 kV, and oxygen particles were accelerated by the 50 V negative bias to bombard the graphenic coating on the plate. The samples GM-0, GM-10, and GM-30 corresponded to the oxygen plasma treatment time of 0 min, 10 min, and 30 min. Based on the characterization of the C/O binding data in XPS (X-ray photoelectron spectroscopy), the experimental samples were intended to represent the pristine state (V_1-0 and V_2-0), oligo-oxygen state (V_1-1 and V_2-1), and poly-oxygen adsorption state (V_1-3 and V_2-4). Induced friction was introduced using a pre-treatment at a load of 0.1 N at 60 rpm for 2 min before the regular friction test. The friction-induced GM-30 sample was named "Induced GM-30" and studied in comparison with other samples. More experimental information can be found in Table S2 in the Supplementary Materials.

A field-emission scanning electron microscope (FE-SEM, Hitachi SU8220, Japan) equipped with energy-dispersive X-ray spectroscopy (EDS) was utilized to examine the surface and cross-sectional morphologies and elemental composition. X-ray diffraction and X-ray photoelectron spectroscopy (XPS, ESCALAB 250xi) were conducted to obtain structural and chemical information. Raman scattering (LabRAM) was carried out to determine the defect density of the graphenic coatings. A three-dimensional profilometer (RTEC UP Dual Model, America) was employed to determine the morphology and roughness of the surface and wear tracks. The ball-on-disk tribometer (MS-T3001) was used to determine the friction under ambient conditions (25 ℃, 50 % RH) with an Al_2O_3 ball with a diameter of 6 mm as the counterpart. The normal friction test was performed at a load of 1 N (0.55 GPa), 382 rpm (or 0.2 m/s), and a wear track radius of 5 mm.

3. Results and discussion

3.1. Evolution of vacancy structures

To investigate the effects of defect engineering performed in the oxygen plasma environment, the possible lubrication problems of graphenic materials are shown in Fig. 1a. Starting from the nature of bonding, we make the following assumptions. For carbon dangling bonds of graphene in high vacuum environments, bonding to oxygen in an excited state may occur, and these excited-state oxygen atoms may be isolated, or the same particles provide multiple binding sites. Investigations are carried out on both single and double carbon vacancy structures. The variation in oxygen binding modes, as illustrated in Fig. 1b, depends on the energy gradients. Negative binding energy demonstrates that sequential binding of oxygen to carbon vacancies occurs in oxygen-rich environments.

At the single vacancy site for active carbon (V_1-0), there is a possibility of preferentially binding with a single oxygen atom (V_1-1) with an adsorption energy of −8.408 eV. Upon prolonged exposure to active oxygen, the structure transitions to binding three oxygen atoms (V_1-3) with a subsequent adsorption energy of −10.204 eV. Regarding the defect structure of the surface double vacancy structure (V_2-0), the adsorption energies of the structure that binds a single oxygen atom (V_2-1) and then evolves to bind four oxygen atoms (V_2-4) are −8.327 eV and −17.034 eV, respectively. As for the non-vacancy regions, oxygen atoms usually do not adsorb stably on the surface of flat multilayer graphene. This indicates similar chemical evolution characteristics for the same types of areas, revealing trends in surface structural changes of defective graphenic materials in the oxygen plasma. Additionally, the oxygen plasma shows etching effects. With the absorption of a certain amount of energy, single carbon vacancy defects can transform into double-atom carbon vacancy defects, with a dissociation energy of 8.136 eV. This transformation process may be induced by the continuous bombardment of high-energy oxygen particles on the surface. Therefore, oxygen plasma treatment of graphenic materials with extensive dangling bond defects transforms the vacancy defects (V_1-0, V_2-0) into oligo-oxygen structures (V_1-1, V_2-1) and eventually poly-oxygen structures (V_1-3, V_2-4), in addition to vacancy expansion.

3.2. Surface friction properties

The evolved microstructure leads to fluctuations in the potential energy surface (PES), significantly affecting the friction. PES calculations were conducted to elucidate the changes in frictional behavior and to simulate the extreme environments of heavy loads in space. Owing to the rugged surface structure caused by adsorption, it is necessary to define the height of the PES plane to the structure surface. Controlling the same contact stresses (σ_{ext}) in the friction tests is an effective way to study the interfacial friction characteristics that are influenced only by surface structural factors [57]. Therefore, the model diagrams in Fig. 2a

and Fig. 2c are constructed and the contact stress is considered as partial derivatives of the interlayer binding energy (E_b) concerning the layer spacing (***z***). The x-y in-plane adjustment of atomic positions, which may reduce the charge redistributions and further decrease the friction between layers, is also considered [58]. Fig. 2b and Fig. 2d show that for controlled high contact stress of 2 GPa, the constant layer spacings (***z***) between the surface layer and friction pair are 3.137 Å, 3.137 Å, and 4.145 Å for V_1-0, V_1-1, and V_1-3, respectively, and 3.137 Å, 3.144 Å, and 3.708 Å for V_2-0, V_2-1, and V_2-4, respectively. The PES relative potential energy surface heights are subsequently set and conditionally calculated based on the layer distance (***z***) of the corresponding structures.

The PES results are shown in Fig. 3 and Fig. 4, indicative of the hexagonal lattice structure of graphene governed by interactions among surface atoms [59]. The distinct disorder in PES is attributed to the vacancies, the adsorbed oxygen atoms, and the orientation of the "armchair" and "zigzag" configurations [60,61]. Paths 1–3 (black dashed arrows) describe the potential sliding directions and Path 2 contains the highest average friction of each surface. Region A corresponds to the lowest potential energy and region B corresponds to the highest along the path. The distance between A and B is marked with a blue line and is subsequently used to calculate the average friction force.

Figs. 3d and 3e exhibit the maximum energy barriers and the energy gradient along Path 2 of the single vacancy structure series. As oxidation proceeds, the structure evolves from V_1-0 to V_1-1 and finally V_1-3, and the corresponding maximum energy barriers are 31.2 meV, 27.4 meV, and 445.1 meV, respectively. As Fig. 3f shows, the average friction forces calculated from Eq. (7) are 16.5 pN, 12.9 pN, and 178.0 pN, respectively. Minkin et al. studied the potential energy surface of twisted single vacancy graphene, showing a maximum point of 28 meV and a maximum average friction of about 12–16 pN [48], suggesting that our results are within reasonable limits. In addition, the modulus of elasticity of the three structures is 940 GPa, 1098 GPa, and 769 GPa, respectively. The higher modulus of elasticity exhibited by V_1-1 helps to prevent wrinkles during sliding and maintains its lowest surface friction. Fig. 4 compares the same elements in -the double vacancy series, where V_2-1 also exhibits the lowest surface average friction (17.0 pN) and the highest modulus of elasticity (849 GPa). This friction law also applies in the low load case (0 GPa case, refer to Figs. S2-S3). The maximum energy barrier and average friction decrease and then increase for both single and double vacancy series, heavy and light loads, corresponding to the oligo-oxygen and poly-oxygen states, respectively. In addition, comparing the same oxygen-bound states, vacancy expansion increases the friction. The high friction generated by the formation of poly-oxygen structure and vacancy expansion is consistent with previous studies reporting an increase in friction with longer oxygen plasma treatment [35,36]. Atomic-level friction measurements and source-based structural evolution studies help to understand the effects of oxidation on *in situ*-grown graphenic materials. The finding that the oligo-oxygen structures reduce friction suggests that controlled oxygen plasma treatment of graphenic materials enhances friction performance. Excessive oxidation causes vacancies to cross the oligo-oxygen state to stabilize to the poly-oxygen state, thus raising the question of how to keep oxidation in the oligo-oxygen, low-friction state. In addition, the binding state of the oxygen atoms needs to be understood.

3.3. Surface microstructures

First-principles calculations were performed to investigate the microstructural features of different surface configurations. Fig. 5 illustrates the microstructure and Fig. 6 describes oxygen binding properties. Vacancies cause the structure to squeeze toward the vacant sites, producing structural torsion and distortion. It is noteworthy that for the oligo-oxygen state of the V_1-1 and V_2-1 structures, oxygen is in a similar bonded state as the neighboring carbon atoms (Fig. 5b). Other studies have also observed the equilibrium structure [62–64]. We suggest that

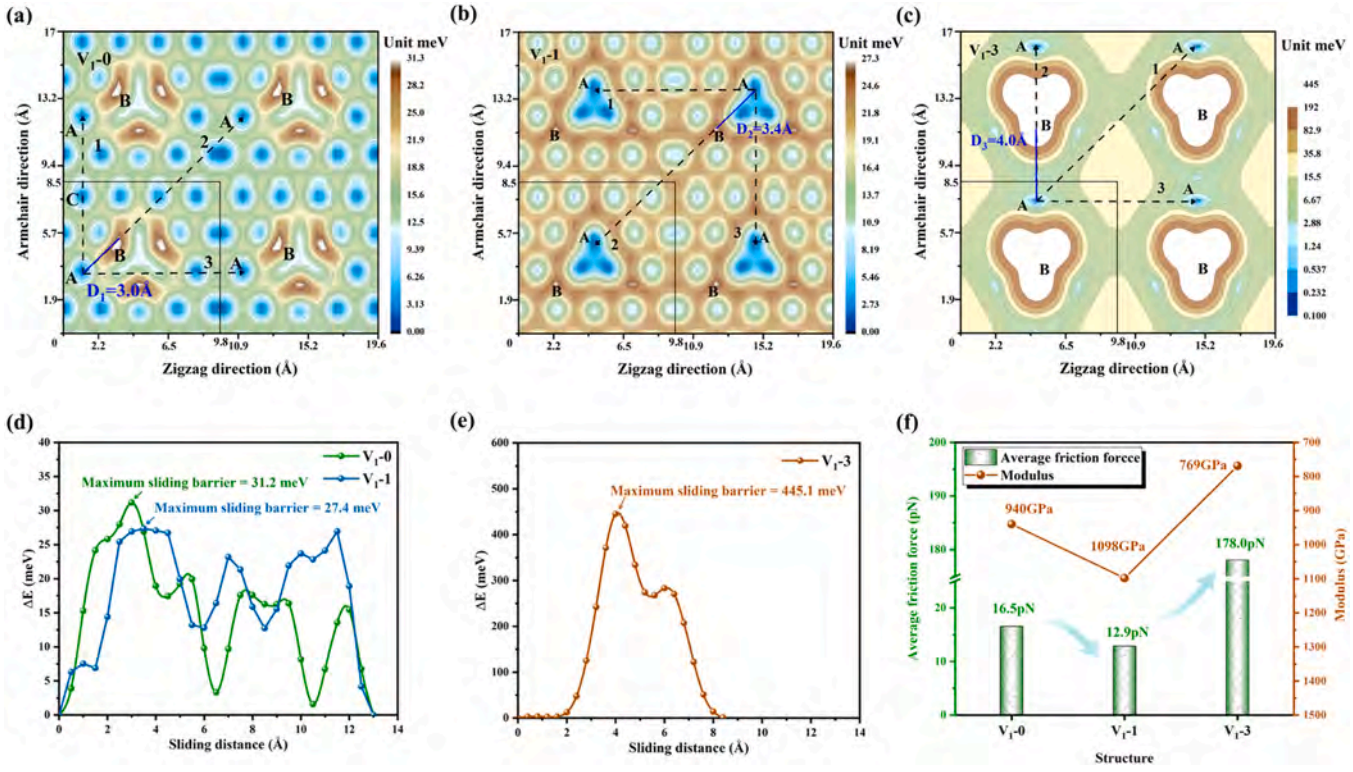

Fig. 3. Friction properties of V_1-0, V_1-1, and V_1-3 at 2 GPa contact stress: Potential energy surface of (a) V_1-0, (b) V_1-1 and (c) V_1-3 (The black number marked next to the dotted line refers to the path number); Maximum energy barrier along Path 2 for (d) V_1-0, V_1-1, and (e) V_1-3. (f) Calculated average friction force and Young's modulus.

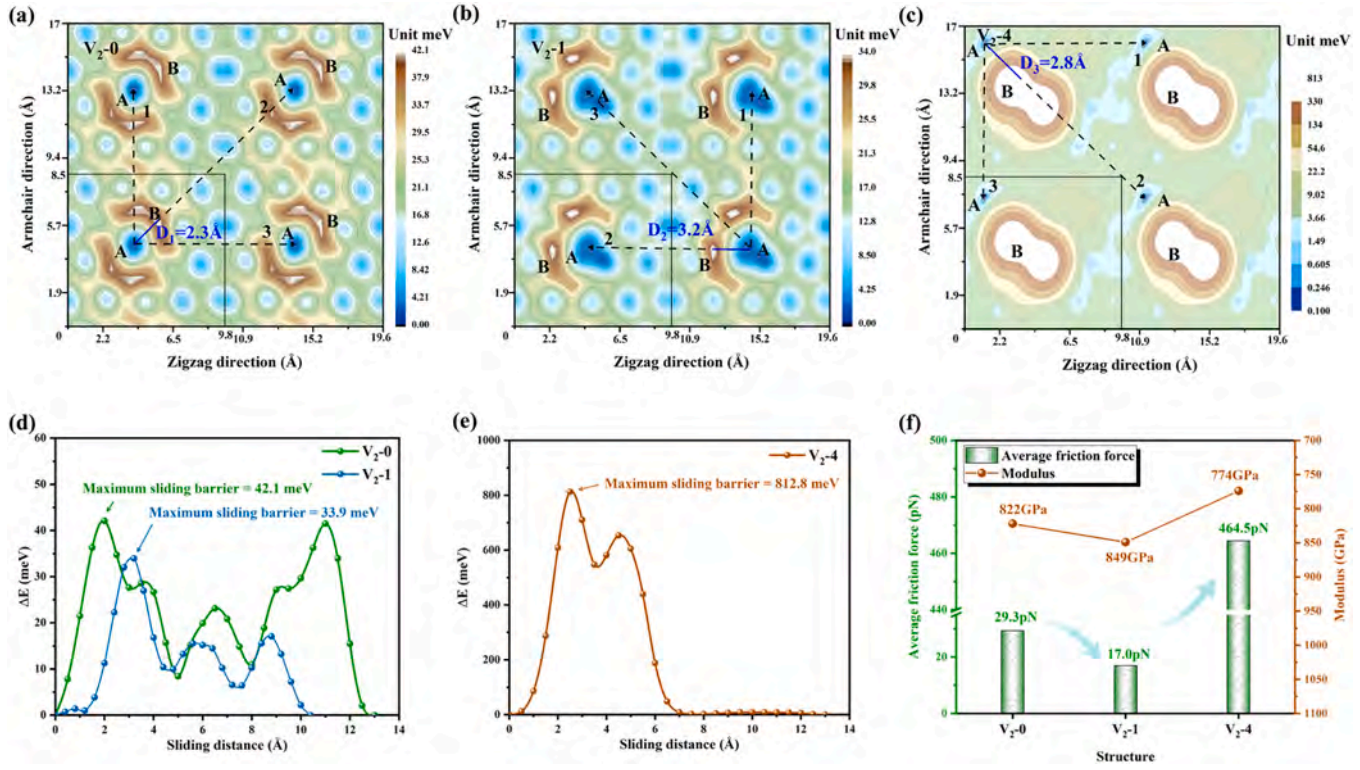

Fig. 4. Friction properties of V_2-0, V_2-1, and V_2-4 at 2 GPa contact stress: Potential energy surface of (a) V_2-0, (b) V_2-1 and (c) V_2-4 (The black number marked next to the dotted line refers to the path number); Maximum energy barrier along Path 2 for (d) V_2-0, V_2-1, and (e) V_2-4. (f) Calculated average friction force and Young's modulus.

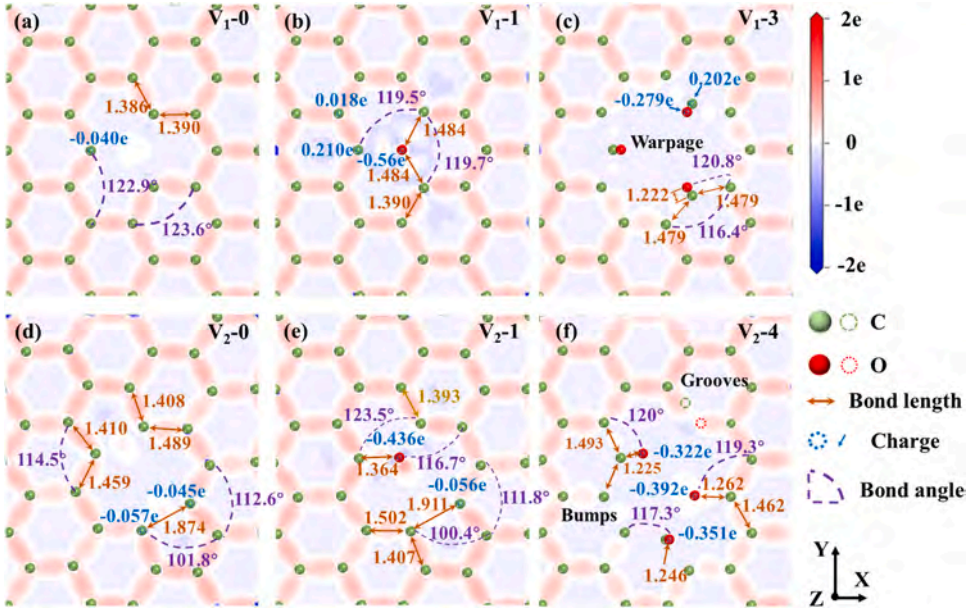

Fig. 5. Surface microstructure. Top view of the (a) V_1-0, (b) V_1-1, (c) V_1-3, (d) V_2-0, (e) V_2-1, and (f) V_2-4 surface. The transfer charge (blue), bond length (brown), and bond angle (purple) were marked in the slices of charge density difference. (Green and red spheres corresponding to carbon and oxygen atoms, respectively. The blue and red regions on the plane indicate electron depletion and accumulation, respectively.).

the introduced O may take sp^2 hybridization, with its 2 s^2 hybridized to two orbitals of single electron-filled $2p^1$, resulting in two C-O σ-bonds of the same nature. The C at the third angle may have taken a special sp^2 hybridization, thus providing the empty orbitals required for coordination bonds to the unhybridized, full-filled p orbitals of O$2p^2$. Three chemically identical C-O bonds are formed upon balancing the electronic structure, exhibiting planar oxygen substitution structures. In addition to the structural configuration, this can also be supported by the diffuse distribution state of the projected density of state (PDOS) for carbon and oxygen atom pairs shown in the upper part of Fig. 6a-b. About the poly-oxygen states, oxygen adsorption causes severe distortions of the structure due to the mutual repulsion of excess atoms. It can

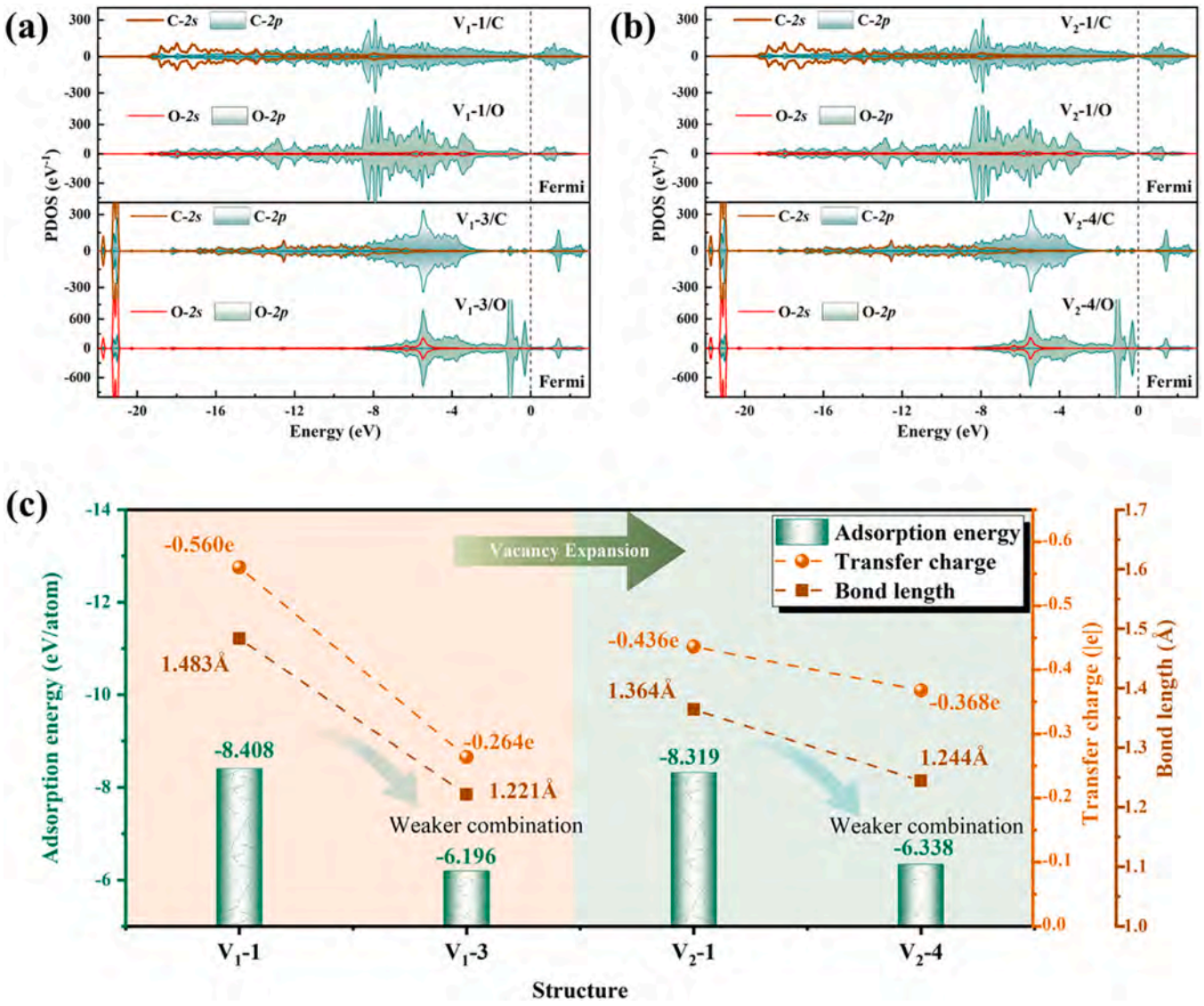

Fig. 6. Oxygen binding properties. (a) PDOS of C-O pairs in V_1-1 and V_1-3; (b) PDOS of C-O pairs in V_2-1 and V_2-4. (c) Comparison of the adsorption energy for each oxygen atom, average transfer charge, and average bond length of V_1-1, V_1-3 (pink background), V_2-1, and V_2-4 (green background).

be observed that warpage on the surface of V_1-3 and bumps and grooves on V_2-4, create a central empty region of the sliced charge difference density in the plane where the center of mass is located. This is one of the reasons why the poly-oxygen state is not conducive to maintaining a smooth, low-friction surface. The region around −21.0 eV and −5.7 eV is shown in the lower half of Fig. 6a-b, which is the result of more pronounced local covalent interactions. Analysis of the PDOS of the carbon-oxygen pairs reveals that the diffuse electronic states are reduced and the overlapping peaks are more concentrated.

As oxidation proceeds, the average adsorption energy of the oxygen atoms, carbon-oxygen bond lengths, and transfer charge vary regularly. As shown in Fig. 6c, the carbon-oxygen bond length of the V_1-1 structure decreases from 1.483 Å to 1.221 Å compared with that of the V_1-3 structure, which is a transition from a C-O single bond determined by σ-bonds and off-domain π-bonds to C═O. Similarly, 1.364 Å of C-O in V_2-1 becomes 1.244 Å in V_2-4 exhibiting a similar bonding transition. The adsorption energy and charge transfer, on the other hand, illustrate the change in the stability of oxygen bonding, and in general, larger absolute values of negative adsorption energy and more charge transfer correspond to a more tightly bonded state. The average oxygen adsorption energy of V_1-1 is −8.408 eV/atom, and the average charge transfer is −0.560|e|, while those of V_1-3 are −6.204 eV/atom and −0.264|e|, respectively. The average oxygen adsorption energies of V_2-1 and V_2-4 show average oxygen adsorption energies of −8.327 eV/atom and −6.340 eV/atom and average charge transfers of −0.436|e| and −0.368|e|, respectively. The decrease in the absolute values of the average adsorption energies and average charge transfer indicates a reduction in the stability of oxygen binding.

3.4. Structural reverse evolution

It is expected to confirm structure-inducing feasibility. Therefore, we created regularly extended surface structures to study the process of friction with alumina spheres, statistically analyzing the oxygen-binding state, as shown in Fig. S4. Fig. 7a-b show snapshots of the poly-oxygen structures (V_1-3 and V_2-4) when they appear as oligo-oxygen structures upon induced friction. It can be seen that the poly-oxygen structures are stably bound on the non-sliding path. Along the sliding path, the surface oxygen structures are regularly laid out, which will lead to regular interaction of the ball with the surface graphene and oxygen structure in the process of friction, causing increasing and decreasing intensity of interaction.

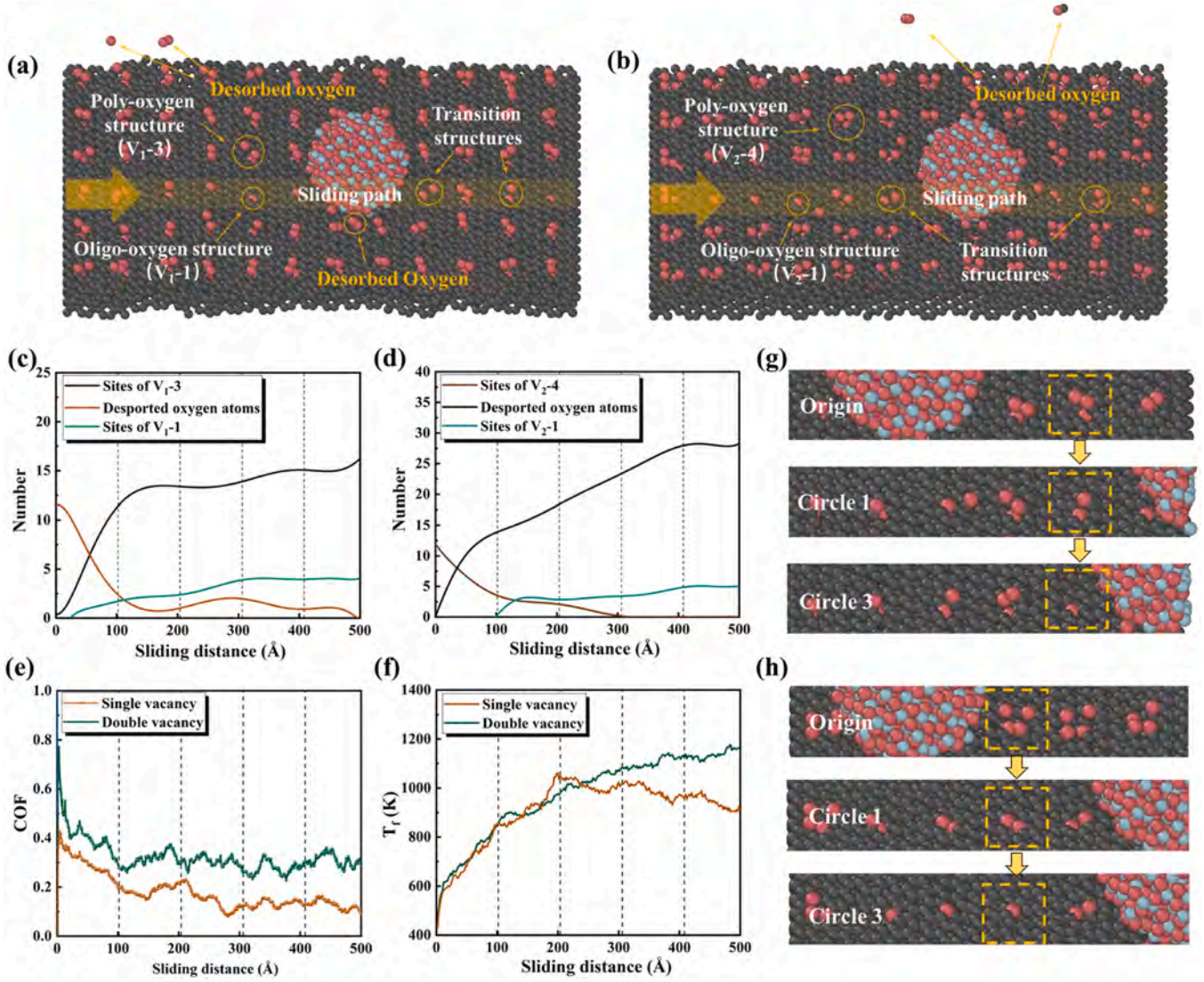

Fig. 7. Reverse evolution process modulated by induced friction. Structural snapshots of (a) single vacancy structure (145 Å sliding distance), and (b) double vacancy structure (150 Å sliding distance) showing the formation of the oligo-oxygen structure. The variation of the number of poly-oxygen structures, desorpted oxygen atoms, and oligo-oxygen structures with the friction sliding distance of (c) single vacancy structure and (d) double vacancy structure. (e) The variation of the coefficient of friction with the friction sliding distance. (f) The variation of the temperature with the friction sliding distance. The gradual transformation of poly-oxygen structure into oligo-oxygen structure during a multiloop sliding process of (g) single vacancy structure and (h) double vacancy structure.

As the induced friction proceeds, the alumina ball interacts with the multi-oxygen structure on the surface, leading to a decrease in the number of sites (V_1-3, V_2-4), an increasing number of sites (V_1-1, V_2-1), and more and more oxygen being desorbed (Fig. 7c-d and Fig. S5). Desorbed oxygen leaves the system mainly in the form of oxygen atoms, oxygen molecules, as well as carbon monoxide and carbon dioxide. Each time the alumina ball slides past 102.26 Å, it enters the next friction cycle (separated by gray dashed lines in the figure). During the first two friction cycles, a large number of transition structures V_1-2, V_2-2, and V_2-3 are generated and gradually transformed into the oligo-oxygen structures of V_1-1, and V_2-1. In the subsequent friction process, the surfaces V_1-1 and V_2-1 play a stabilizing role in reducing friction, the temperature tends to be smoothed and the friction coefficient tends to be stabilized. The complete friction process is shown in the video Figs. S6-S7.

Fig. 7g-h focuses on the same region (left-numbered 6 oxygen regions for single vacancies and right-numbered 6 oxygen regions for double vacancies), in which the initial poly-oxygen structure, the transition structures after the first induced friction, and the oligo-oxygen structure after the third induced friction are gradually formed. It suggests that the transformation of the structure may need to be treated with multiple induced friction circles before it occurs, but it may ultimately stabilize at the less-oxygen structure. This is in agreement with the predictions of the DFT calculations on the oxygen binding strength.

3.5. Tribological experiments

The simulation results confirm the forward evolution and reverse evolution of graphenic vacancies by oxygen plasma treatment and induced friction. We applied the mechanism in a macroscopic environment to inform practical applications. Graphenic material samples with moderate defects prepared by HFCVD were treated in the oxygen plasma, and the relevant friction experiments and characterization were carried out to investigate the application of the mechanism in atmospheric environments. Fig. S8. displays the surface morphology of the microstructure by scanning electron microscopy (SEM). Initially, the GM-0 shows separated islands, protrusions, valleys, and edge effects with a roughness of 580 nm. After short-term oxygen plasma treatment,

GM-10 (Ra=177 nm) shows a better continuity due to the passivation of the atomic structure. Golda-Cepa et al. found that oxygen plasma treatment of graphenic materials can introduce oxidized functional groups while maintaining an intact surface morphology [65]. However, prolonged oxygen plasma etching damages the surface structure, with isolated structures increasing again in GM-30 Ra = 386 nm). The induced friction traces at small loads produce suitable sliding tracks, as shown in Fig. S8h. It is advantageous to induce the formation of a turbostratic carbon structure [66], a self-orientating graphenic film [67], a friction-transferring film [68], or other friction-reducing structures in a low-loss form before harsh conditions. The roughness of the induced friction tracks on the Induced GM-30 structure is 31 nm, and controlling appropriate roughness facilitates the formation of locally loose and wrinkled contact interfaces and even smooth surfaces to reduce the contact area while promoting interlayer sliding.

The tribological properties of the graphenic materials are determined by ball-on-disc friction tests, as shown in Fig. 8a. The average coefficients of friction (COF) decrease from 0.1675 for the GM-0–0.1163 for GM-10 and then increase to 0.3854 for GM-30. The GM-10, an example of oligo-oxygen structures, exhibits low friction properties and better wear resistance over a longevity of 360 m. It is capable of meeting the needs of equipment operating in an oxygen plasma environment, and the properties are excellent compared to the majority of graphenic coatings on the macroscale under ambient conditions reported to date [69–75]. Induced friction that applied to Induced GM-30 results in a 62.9 % reduction in COF from 0.3854 to 0.1426. As shown in the green dotted box area in Fig. 8a, the COF (0.083) of the Induced GM-30 is as low as in GM-10 during the initial phase of friction, showing similar friction properties.

The EDS analysis of the friction tracks reveals that GM-30 has more Co/W/Al and less C (Fig. 8b), indicating that graphenic material is more severely abraded and delaminated, and the wear condition is severe. Figs. 8c1-c4 show different degrees of plastic deformation, wear debris, grooves, and delamination during sliding of the wear tracks. In particular, the coating undergoes severe abrasive and adhesion wear due to repeated crushing, deformation, agglomeration, and embedding of wear debris in the over-oxidized GM-30 sample. This phenomenon may be attributed to the increase in the hard composition of NiO with oxidation time and the corresponding decrease in friction stability. On the other hand, in GM-10 and Induced GM-30, the coatings exhibit smoother wear trajectories and reduced wear (Figs. 8c3–4). The 3D profiles and line scans are shown in Fig. 8d-g. The wear track widths of the over-oxidized GM-30 are significantly larger than those of the other samples. The wear mechanism of graphenic samples can be ascribed to surface synergy, abrasion, and oxidative wear effects.

3.6. Characterization of graphenic samples

The Raman spectra (Fig. S9) show distinct D, G, and 2D peaks, indicating the transformation of defective graphene into graphene oxide with different disordered degrees as a result of oxygen plasma treatment. The XPS C1*s* spectrum (Fig. 9a) shows the C-C, C-O, and C═O functional groups at 284.80 eV, 286.46 eV, and 288.74 eV [76], respectively. As oxidation proceeds, the C═O contents in GM-0, GM-10, and GM-30 increase from 5.6 % to 8.3 % and 13.3 %, indicating increased C═O content due to oxidation treatment, especially for graphenic materials with more vacancies where each vacancy introduces multiple C═O bonds. This may prove that the poly-oxygen structures (V_1-3 and V_2-4, containing more C═O) in the simulation correspond to GM-30. In addition, friction induction increases the content of C-O as the C═O bond decreases to 8.9 %. The statistical distributions from the surface and the wear track in Fig. S9 indicate that the structures in the induced friction samples exhibit comparable characteristics to those of graphite oxide. In Fig. 9c, the GM-10 and Induced GM-30 structures have a greater proportion of C-O bonds, with ratios of 10.5 % and 13.8 %, respectively, which is consistent with the nature of the low-friction oligo-oxygen structures (V_1-1 and V_2-1). These may exemplify the reverse evolution found by simulations, in which C═O bonds are induced to convert to C-O bonds by conditional induced friction.

Figs. 9b, 9d depicts the spectrum of Ni 2*p*, in which the peaks at 852.84 eV and 870.06 eV correspond to Ni^0 $2p_{3/2}$ and Ni^0 $2p_{1/2}$. The peaks at 856.23 eV and 873.97 eV arise from Ni $2p_{3/2}$ and Ni $2p_{1/2}$ of

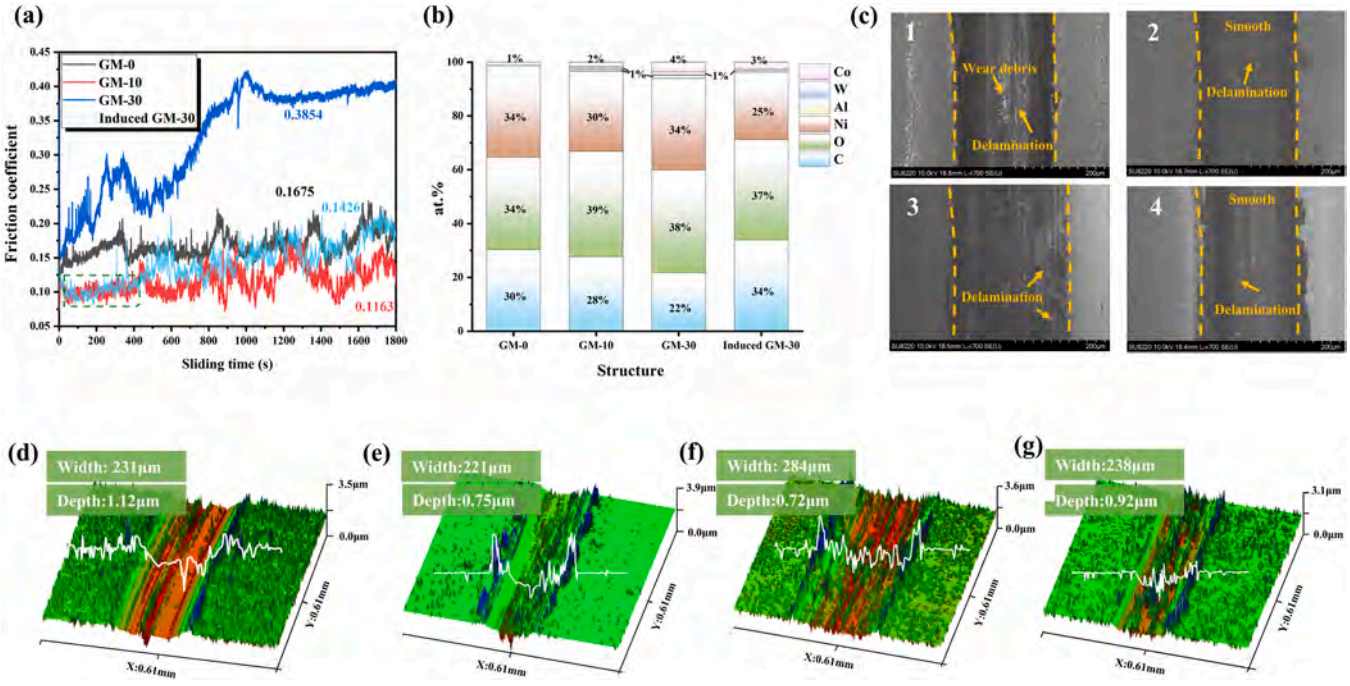

Fig. 8. Tribological properties and characterization of graphenic coatings for different oxidation time or friction treatments: (a) Friction coefficients as a function of sliding time; (b) Chemical composition of the wear tracks; (c) Surface morphology of the wear tracks of (1) GM-0, (2) GM-10, (3) GM-30, and (4) Induced GM-30; Three-dimension morphology mappings and line scans of the wear tracks of (d) GM-0, (e) GM-10, (f) GM-30, (g)Induced GM-30. (The samples GM-0, GM-10, and GM-30 corresponded to the oxygen plasma treatment time of 0 min, 10 min, and 30 min. The sample Induced GM-30 indicates the GM-30 after induced friction).

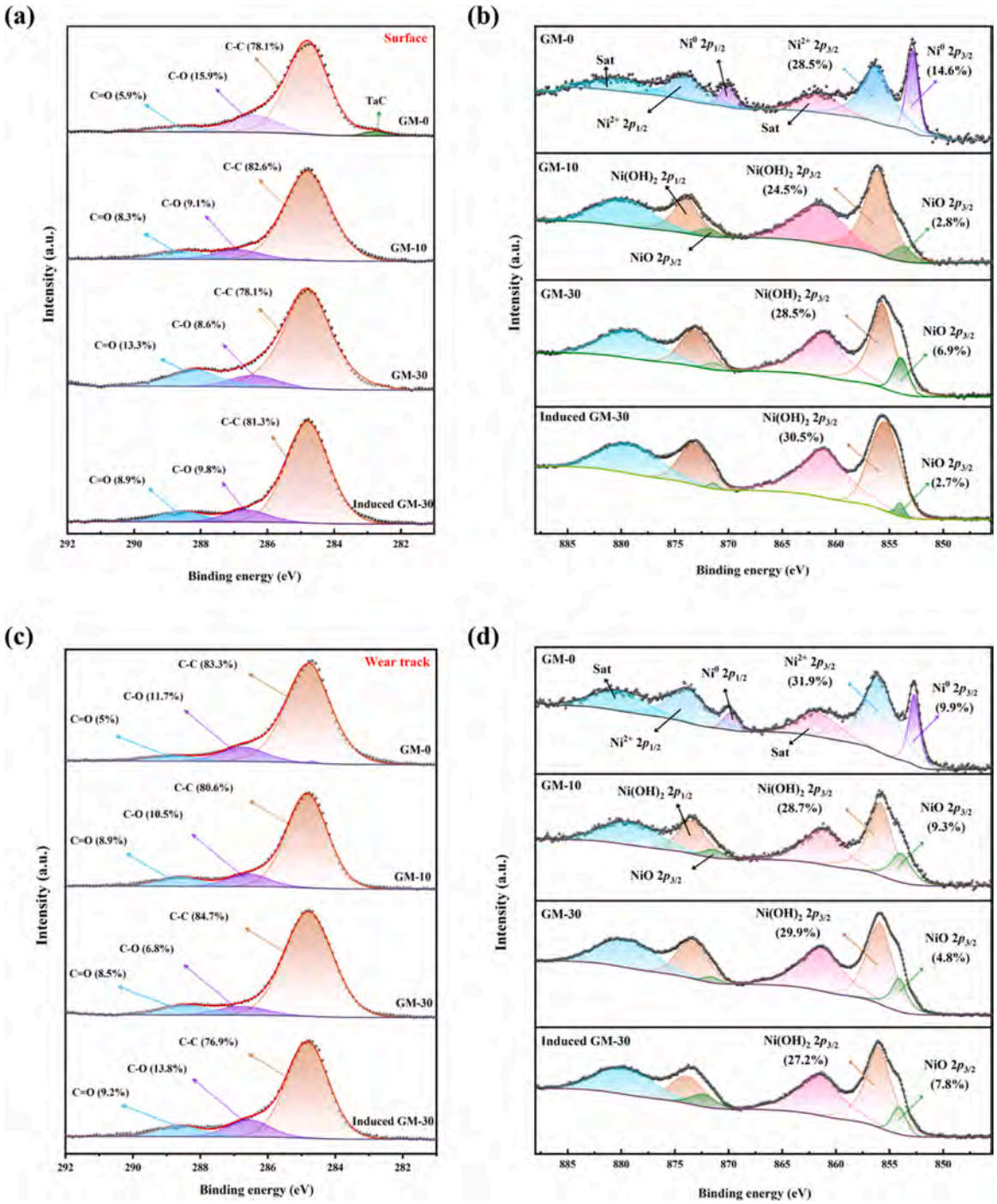

Fig. 9. High-resolution XPS spectra with Gaussian-Lorentzian fits of (a) C 1 *s*, (b) Ni 2*p* before friction, and (c) C 1 *s*, and (d) Ni 2*p* after friction.

Ni^{2+}, and the satellite peaks emerge at 861.54 eV and 880.02 eV. The peaks of NiO and $Ni(OH)_2$ are fitted for further analysis. The NiO peaks at 853.93 eV and 871.35 eV correspond to Ni $2p_{3/2}$ and Ni $2p_{1/2}$, while the peaks at 855.65 eV and 873.08 eV arise from Ni $2p_{3/2}$ and Ni $2p_{1/2}$ of $Ni(OH)_2$. As oxidation progresses, the Ni^0 peak transitions to Ni^{2+} (mainly $Ni(OH)_2$), and the NiO and $Ni(OH)_2$ contents gradually increase. The friction may introduce water molecules into the surface reaction under experimental conditions, thus causing a consistent increase in the -OH, and -O content. Water molecules increase interfacial friction in our high-humidity friction experimental conditions mainly through the formation of hydrogen bonds [77,78], whereas vacancy and oligo-oxygen structures are less affected due to the lack of binding sites. The experiments aim to inform applications.

3.7. Friction dominance mechanisms

Fig. 10 summarizes the roles played by oxygen plasma and induced friction in modulating oxidation at the atomic scale. On the surface of an infinitely extended graphenic coating, a series of structural evolutions will take place on its vacancies. In the context of oxygen plasma treatment, due to the presence of unpaired sp^2 orbitals for carbon atoms near the vacancy structure, a shorter treatment time will introduce C-O, which passivates the surface and reduces the potential surface undulation, thus reducing surface friction. On the contrary, prolonged treatment causes severe surface etching, probably induces vacancy expansion, and introduces a large number of C═O bonds. These C═O repel each other, causing a rugged structure, a rise in surface activity,

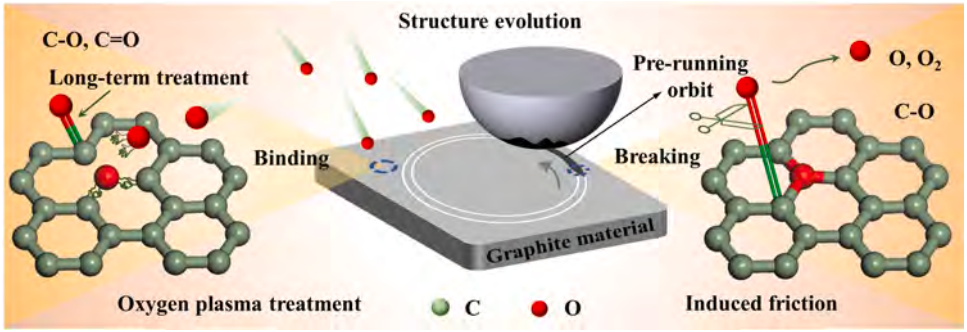

Fig. 10. Schematic diagram of the bi-directional evolution of the structure due to oxygen plasma treatment and induced friction.

and an increase in friction. The hydrophilicity and work function of the surface may also be enhanced as a result [65,79]. Through induced friction, a reverse evolution of the structure may occur. The friction pairs interact violently with the rugged C═O structures, disconnecting the weaker C═O and inducing the re-formation of stable C-O bonds, thus controlling the degree of oxidation. These planar C-O bonds form a flat, low electro-activity surface, restoring the structure to a low-friction state.

It is challenging to establish a direct relationship between friction mechanisms established by density functional theory and molecular dynamics studies with macroscopic friction applications. The reason is that the latter is usually a complex process involving a combination of multiple mechanisms and deviations from simulated conditions. Herein, we aim to illustrate the evolution and reserve evolution of graphenic vacancy structures in oxygen plasma environments through atomic-scale studies and macroscopic experimental applications, and ultimately provide mechanistic explanations and effective solutions for possible friction and wear problems of graphenic coatings in facing plasma treatment.

4. Conclusions

Based on density-functional theory (DFT) and molecular dynamics (MD) calculations, we investigate the forward evolution from graphenic vacancy to oligo-oxygen structures and poly-oxygen structures with oxygen plasma treatment, predict friction-reduced states, and confirm the friction increase due to long-time treatment. We also propose a means of reverse evolution from the poly-oxygen structures to the oligo-oxygen structures through induced friction for precise structural regulation. We explore these processes at the atomic level and apply the findings experimentally to gain insight into the macroscopic manifestations of atomic-scale mechanisms, thereby offering insights into the lubricating properties and the mechanisms of graphenic coatings in facing extreme treatment, including oxygen plasma encountered in semiconductor processing and space exploration.

Statement of Originality

The authors declare that the work described was original research that has not been published previously, and not under consideration for publication elsewhere, in whole or in part.

CRediT authorship contribution statement

Paul K. Chu: Resources, Project administration, Funding acquisition. **Jing Wu:** Writing – review & editing, Methodology, Investigation, Formal analysis. **Yi Wu:** Writing – review & editing, Methodology, Conceptualization. **Fenghua Su:** Supervision, Resources. **Guoliang Tang:** Software, Methodology. **Shuyu Fan:** Writing – review & editing, Writing – original draft, Software, Methodology, Investigation, Data curation, Conceptualization. **Yinong Chen:** Writing – review & editing, Writing – original draft, Software, Methodology, Investigation, Data curation, Conceptualization. **Hu Zhang:** Writing – review & editing, Supervision, Software, Methodology. **Shu Xiao:** Supervision, Resources, Project administration, Funding acquisition.

Declaration of Competing Interest

The authors declare that they have no known competing financial interests or personal relationships that could have appeared to influence the work reported in this paper.

Acknowledgments

We acknowledge the financial support from National Natural Science Foundation of China (Nos.52375182 & 52005187), Natural Science Foundation of Guangdong Province (No.2023A1515012308), Fundamental Research Funds for the Central Universities (No.2023ZYGXZR030), Basic and Applied Basic Research Foundation of Guangzhou (No.2024A04J3821), and City University of Hong Kong Donation Research Grants (DON-RMG 9229021 and 9220061).

Appendix A. Supporting information

Supplementary data associated with this article can be found in the online version at doi:10.1016/j.triboint.2025.110529.

Data availability

Data will be made available on request.

References

[1] Zhao J, Huang YY, He YY, Shi YJ. Nanolubricant additives: a review. Friction 2021;9:891–917.
[2] Jin B, Zhao J, He YY, Chen GY, Li YL, Zhang CH, et al. High-quality ultra-flat reduced graphene oxide nanosheets with super-robust lubrication performances. Chem Eng J 2022;438:135620.
[3] Liu YF, Ge XY, Li JJ. Graphene lubrication. Appl Mater Today 2020;20:100662.
[4] Erdemir A, Ramirez G, Eryilmaz QL, Narayanan B, Liao YF, Kamath G, et al. Carbon-based tribofilms from lubricating oils. Nature 2016;536:67–71.
[5] Fan SY, Chen YN, Wu J, Xiao S, Chen GH, Chu PK. Structure, superlubricity, applications, and chemical vapor deposition methods of graphene solid lubricants. Tribol Int 2024;198:109896.
[6] Jin B, Chen GY, Zhao J, He YY, Huang YY, Luo JB. Improvement of the lubrication properties of grease with Mn3O4/graphene (Mn3O4#G) nanocomposite additive. Friction 2021;9:1361–77.
[7] Jin B, Zhao J, Chen GY, He YY, Huang YY, Luo JB. In situ synthesis of Mn3O4/graphene nanocomposite and its application as a lubrication additive at high temperatures. Appl Surf Sci 2021;546:149019.
[8] Shi QQ, Zong Q, Fu SY, Dunlop MW, Pu ZY, Parks GK, et al. Solar wind entry into the high-latitude terrestrial magnetosphere during geomagnetically quiet times. Nat Commun 2013;4:1466.
[9] Wu Y, Xiao S, Chen YN, Dong WL, Liu JC, Huang Y, et al. Oxygen plasma-assisted magnetron sputtering deposition of non-stoichiometric Y2O3 films: Influence of oxygen vacancies on etching resistance. Surf Coat Technol 2024;494:131448.

[10] Hug D, Zihlmann S, Rehmann MK, Kalyoncu YB, Camenzind TN, Marot L, et al. Anisotropic etching of graphite and graphene in a remote hydrogen plasma. npj 2D Mater Appl 2017:21.
[11] Yang C, Wang CY, Sheng LY, Zhao CC, Chen PH, Ouyang WT, et al. Improved lubricating and corrosion resistance of MAO coatings on ZK61 Mg alloy by co-doping with graphite and nano-zirconia. J Mater Res Technol 2024;33:2275–91.
[12] Wang Chenyu, Sun Mingshan, Yang* Chao, Wang Haiyang, Wang Jie, Mao Lin, et al. Degradation behavior of pure Mg in the physiological medium and growth mechanism of surface corrosion product films. J Magnes Alloy 2024;4:35.
[13] Xu WN, Qin Z, Chen C, Kwag HR, Ma Q, Sarkar A, et al. Ultrathin thermos-responsive self-folding 3D graphene. Sci Adv 2017;3:e1701084.
[14] Jin B, Chen GY, Zhao J, He YY, Li YL, Luo JB. Coupling effect of boundary tribofilm and hydrodynamic film. Cell Rep Phys Sci 2022;3:10078.
[15] Yin JB, Tan C, Barcons-Ruiz D, Torre I, Watanabe K, Taniguchi T, et al. Tunable and giant valley-selective Hall effect in gapped bilayer graphene. Science 2022; 375:1398–402.
[16] Carrasco DF, Paredes JI, Villar-Rodil S, Suarez-García F, Martínez-Alonso A, Tascon JMD. An electrochemical route to holey graphene nanosheets for charge storage applications. Carbon 2022;195:57–68.
[17] Zhai WZ, Srikanth N, Kong LB, Zhou K. Carbon nanomaterials in tribology. Carbon 2017;119:150–71.
[18] Chen XC, Li JJ. Superlubricity of carbon nanostructures. Carbon 2020;158:1–23.
[19] Liu S, Chevali VS, Xu ZG, Hui D, Wang H. A review of extending performance of epoxy resins using carbon nanomaterials. Compos B Eng 2018;136:197–214.
[20] Wang L, Tieu AK, Ma M, Li JQ, Hai GJ, Zhu HT. Potential application of graphene nanoplatelets as a high temperature lubricant for hot rolling. Friction 2022;10(11): 1810–23.
[21] Ji ZJ, Zhang L, Xie GX, Xu WH, Guo D, Luo JB, et al. Mechanical and tribological properties of nanocomposites incorporated with two dimensional materials. Friction 2020;8(5):813–46.
[22] Yang G, Li LH, Lee WB, Ng MC. Structure of graphene and its disorders: a review. Sci Technol Adv Mater 2018;19:613–48.
[23] Malekpour H, Ramnani P, Srinivasan S, Balasubramanian G, Nika DL, Mulchandani A, et al. Thermal conductivity of graphene with defects induced by electron beam irradiation. Nanoscale 2016;8(30):14608–16.
[24] Tapia A, Peón-Escalante R, Villanueva C, Avilés F. Influence of vacancies on the elastic properties of a graphene sheet. Comput Mater Sci 2012;55:255–62.
[25] Acik M, Chabal YJ. Nature of graphene edges: a review. Jpn J Appl Phys 2011;50: 070101.
[26] Batzill M. The surface science of graphene: Metal interfaces, CVD synthesis, nanoribbons, chemical modifications, and defects. Surf Sci Rep 2012;67:83–115.
[27] Rasool HI, Ophus C, Klug WS, Zettl A, Gimzewski JK. Measurement of the intrinsic strength of crystalline and polycrystalline graphene. Nat Commun 2013;4:2811.
[28] Zhang JF, Zhao JJ, Lu JP. Intrinsic strength and failure behaviors of graphene grain boundaries. ACS Nano 2012;6(3):2704–11.
[29] Fan SY, Chen YN, Xiao S, Shi KJ, Meng XY, Lin SS, et al. In situ self-adaptive growth of graphene coatings on hard substrates via competitive NiCo catalysis reaction. Carbon 2024;216:118561.
[30] Dong YL, Wu XW, Martini A. Atomic roughness enhanced friction on hydrogenated graphene. Nanotechnology 2013;24:375701.
[31] Yang C, Sun MS, Huang AH, Chen PH, Chu PK. Optimization of tribological properties and corrosion resistance of MAO coatings on LY12 aluminum alloy by co-doping with graphite particles and in situ formation of zinc phosphate. Ceram Int 2024;50:46018–31.
[32] Li QY, Liu X, Kim S, Shenoy VB, Sheehan PE, Robinson JT, et al. Fluorination of graphene enhances friction due to increased corrugation. Nano Lett 2014;14: 5212–7.
[33] Ko J, Kwon S, Byun I, Choi JS, Park BH, Kim Y, et al. Nanotribological properties of fluorinated, hydrogenated, and oxidized graphenes. Tribol Lett 2013;50:137–44.
[34] Fan SY, Xiao S, Lin SS, Su FH, Su YF, Chu PK. Macroscale superlubricity and durability of in situ grown hydrogenated graphene coatings. Chem Eng J 2023;459: 141521.
[35] Gajurel P, Kim M, Wang Q, Dai WT, Liu HT, Cen C. Vacancy-Controlled Contact Friction in Graphene. Adv Funct Mater 2017;27:1702832.
[36] Yuan R, Li P, Chen L, Yuan J, Xu BH, Sun GQ, et al. Effects of grafting oxygen atoms on the tribological properties of graphene: molecular dynamics simulation and experimental analysis. Appl Surf Sci 2020;528:147045.
[37] Jia PF, Pan FM, Chen TH. Effect of oxygen plasma etching on graphene's mechanical and electrical properties. IOP Conf Ser: Mater Sci Eng 2017;182: 012030.
[38] Zeng XZ, Peng YT, Lang HJ, Liu L. Controllable nanotribological properties of graphene nanosheets. Sci Rep 2017;7:41891.
[39] Delley B. An all-electron numerical method for solving the local density functional for polyatomic molecules. J Chem Phys 1990;92(1):508–17.
[40] Perdew JP, Burke K, Ernzerhof M. Generalized gradient approximation made simple. Phys Rev Lett 1997;78(7). 1396-1396.
[41] Perdew JP, Chevary JA, Vosko SH, Jackon KA, Pederson MR, Singh DJ, et al. Atoms, molecules, solids, and surfaces: applications of the generalized Gradient approximation for exchange and vorrelation. Phys Rev B 1992;46(11):6671–87.
[42] Grimme S. Semiempirical GGA-type density functional constructed with a long-range dispersion correction. J Comput Chem 2006;27(15):1787–99.
[43] Wang YF, He MJ, He WH, Niu Y, Lu ZB. The influences of atom relaxation on the DFT-calculated friction properties of the h-BN/h-BN and Gr/Gr interfaces. Tribol Int 2022;173:107586.
[44] Sun JH, Zhang X, Du SY, Pu JB, Wang Y, Yuan YP, et al. Charge Density. Evol Gov Interfacial Frict, J Am Chem Soc 2023;145:5536–44.
[45] Zhong W, Tomanek D. First-Principles Theory of Atomic-Scale Friction. Phys Rev Lett 1990;64:3054.
[46] Cahangirov S, Ataca C, Topsakal M, Sahin H, Ciraci S. Frictional Figures of Merit for Single Layered Nanostructures. Phys Rev Lett 2012;108:126103.
[47] Minkin AS, Lebedeva IV, Popov AM, Knizhnik AA. Atomic-scale defects restricting structural superlubricity: *Ab initio* study on the example of the twisted graphene bilayer. Phys Rev B 2021;104:075444.
[48] Zhang BZ, Zhang GG, Cheng ZW, Ma F, Lu ZB. Atomic-scale friction adjustment enabled by doping-induced modification in graphene nanosheet. Appl Surf Sci 2019;483:742–9.
[49] Hu JB, Jian XG, Yang T, Peng XY. Investigation on the interface characteristic between WC(001) and diamond(111) by first-principles calculation. Diam Relat Mater 2022;123:108864.
[50] Dai PL, Wei ZC, Chen LZ, Liu Y. Adsorption of butyl xanthate on arsenopyrite (0 0 1) and Cu^{2+}-activated arsenopyrite (0 0 1) surfaces: a DFT study. Chem Phys 2022;562:111668.
[51] Hong S, Van Duin ACT. Atomistic-scale analysis of carbon coating and its effect on the oxidation of aluminum nanoparticles by ReaxFF-molecular dynamics simulations. J Phys Chem C 2016;120:9464–74.
[52] Amiri N, Ghasemi JB, Behnejad H. Atomistic insights into the protection failure of the graphene coating under the hyperthermal impacts of reactive oxygen species: ReaxFF-based molecular dynamics simulations. Appl Surf Sci 2021;554:149606.
[53] Zhang XF, Zheng PR, Ma YJ, Jiang YY, Li H. Atomic-scale understanding of oxidation mechanisms of materials by computational approaches: A review. Mater Des 2022;217:110605.
[54] Jiang Y, Deng SL, Hong S, Zhao JH, Huang SD, Wu C, et al. Energetic performance of optically activated aluminum/graphene oxide composites. ACS Nano 2018;12: 11366–75.
[55] Munir KS, Wen C, Li Y. Carbon nanotubes and graphene as nanoreinforcements in metallic biomaterials: a review. Adv Biosyst 2019;3(3):1800212.
[56] Fan K, Chen XY, Wang X, Liu XK, Liu Y, Lai WC, et al. Toward excellent tribological performance as oil-based lubricant additive: particular tribological behavior of fluorinated graphene. ACS Appl Mater Interfaces 2018;10:28828–38.
[57] Liu YH, Zhang H, Liu T, Wang XW, Luo YY, Zhu XH. Exploring the effects of water content on friction behavior and mechanism of DLC films in oil production environment based on molecular dynamics simulation and first-principles calculations. Diam Relat Mater 2023;139:110294.
[58] He MJ, Wang YF, He WH, Niu Y, Lu ZB. In-plane adjustment of atomic positions and layer-dependent friction in 2D materials. Appl Surf Sci 2023;620:156810.
[59] Zhang XW, Qi WH, Tang KW, Ru GL, Liu WM. First-principles calculations combined with friction models to predict the moire pattern effect on the interlayer friction of two-dimensional materials. Tribol Int 2024;191:109087.
[60] Radchenko TM, Tatarenko VA, Cuniberti G. Effects of external mechanical or magnetic fields and defects on electronic and transport properties of graphene. Mater Today: Proc 2021;35:523–9.
[61] Renteria JD, Ramirez S, Malekpour H, Alonso B, Centeno A, Zurutuza A, et al. Strongly anisotropic thermal conductivity of free-standing reduced graphene oxide films annealed at high temperature. Adv Funct Mater 2015;25:4664–72.
[62] Qi XJ, Guo X, Zheng CG. Density functional study the interaction of oxygen molecule with defect sites of graphene. Appl Surf Sci 2012;259:195–200.
[63] Duch J, Mazur M, Golda-Cepa M, Podobinski J, Piskorz W, Kotarba A. Insight into the modification of electrodonor properties of multiwalled carbon nanotubes via oxygen plasma: surface functionalization versus amorphization. Carbon 2018;137: 425–32.
[64] Zhu XH, Liu K, Lu ZB, Xu YP, Qi SS, Zhang GG. Effect of oxygen atoms on graphene: Adsorption and doping. Phys E 2020;117:113827.
[65] Golda-Cepa M, Kumar D, Bialoruski M, Lasota S, Madeja Z, Piskorz W, et al. Functionalization of graphenic surfaces by oxygen plasma toward enhanced wettability and cell adhesion: experiments corroborated by molecular modelling. J Mater Chem B 2023;11:4946–57.
[66] Carina EM, Andreas K, Martin D, Michael M. Humidity-dependent lubrication of highly loaded contacts by graphite and a structural transition to turbostratic carbon. Nat Commun 2022;13:5958..
[67] Li PP, Ju PF, Ji L, Li HX, Liu XH, Chen L, et al. Toward robust macroscale superlubricity on engineering steel substrate. Adv Mater 2020;32:2002039.
[68] Yin X, Zhang J, Luo T, Cao BQ, Xu JX, Chen XC, et al. Tribochemical mechanism of superlubricity in graphene quantum dots modified DLC films under high contact pressure. Carbon 2021;173:329–38.
[69] Berman D, Erdemir A, Sumant AV. Few layer graphene to reduce wear and friction on sliding steel surfaces. Carbon 2013;54:454–9.
[70] Bhowmick S, Banerji A, Alpas AT. Friction reduction mechanisms in multilayer graphene sliding against hydrogenated diamond-like carbon. Carbon 2016;109: 795–804.
[71] Zhang ZY, Du YF, Huang SL, Meng FN, Chen LL, Xie WX, et al. Macroscale superlubricity enabled by graphene-coated surfaces. Adv Sci 2020;7(4):1903239.
[72] Li JJ, Ge XY, Luo JB. Random occurrence of macroscale superlubricity of graphite enabled by tribo-transfer of multilayer graphene nanoflakes. Carbon 2018;138: 154–60.
[73] Singh S, Chen XC, Zhang CH, Gautam RK, Tyagi R, Luo JB. Nickel-catalyzed direct growth of graphene on bearing steel (GCr15) by thermal chemical vapor deposition and its tribological behavior. Appl Surf Sci 2020;502:144135.
[74] Xiang L, Shen QQ, Zhang Y, Bai W, Nie CY. One-step electrodeposited Ni-graphene composite coating with excellent tribological properties. Surf Coat Technol 2019; 373:38–46.
[75] Shi Z, Shum P, Wasy A, Zhou ZF, Li LKY. Tribological performance of few layer graphene on textured M2 steel surfaces. Surf Coat Technol 2016;296:164–70.

[76] Table of elements: X-ray photoelectron spectroscopy of atomic elements (ThermoFisher scientific 2018) [online] https://www.thermofisher.cn/cn/zh/home/materials-science/learning-center/periodic-table.html.
[77] Gao X, Chen L, ji L, Liu X, Li H, Zhou H, et al. Humidity-sensitive macro-scopic lubrication behavior of an as-sprayed graphene oxide coating. Carbon 2018;140:124–30.
[78] Wang MJ, Wang A, Zhao WJ, Meng XK, Peng XD, Wang JQ. The ion diffusion-directed self-assembled graphene oxide coating and its synergistic lubrication mechanism against environmental moisture. Tribol Int 2024;191:109182.
[79] Białoruski M, Kumar D, Gołda-Cępa M, Piskorz W, Kotarba A. Work function of the oxygen functionalized graphenic surfaces – Integral experimental and theoretical approach. Appl Surf Sci 2022;597:153671..

Supplementary Materials

Bi-directional Evolution of Graphenic Vacancy Structure in Oxygen Plasma Treatment

Yinong Chen[a,1], Shuyu Fan[a,1], Shu Xiao[a,*], Hu Zhang[a], Yi Wu[a], Jing Wu[a], Guoliang Tang[a], Fenghua Su[a], Paul K. Chu[b]

[a] School of Mechanical & Automotive Engineering, South China University of Technology, Guangzhou 510641, China

[b] Department of Physics, Department of Materials Science and Engineering, and Department of Biomedical Engineering, City University of Hong Kong, Tat Chee Avenue, Kowloon, Hong Kong, China

[*] Corresponding authors: xiaos@scut.edu.cn (S. Xiao)

[1] These authors contributed equally to this work

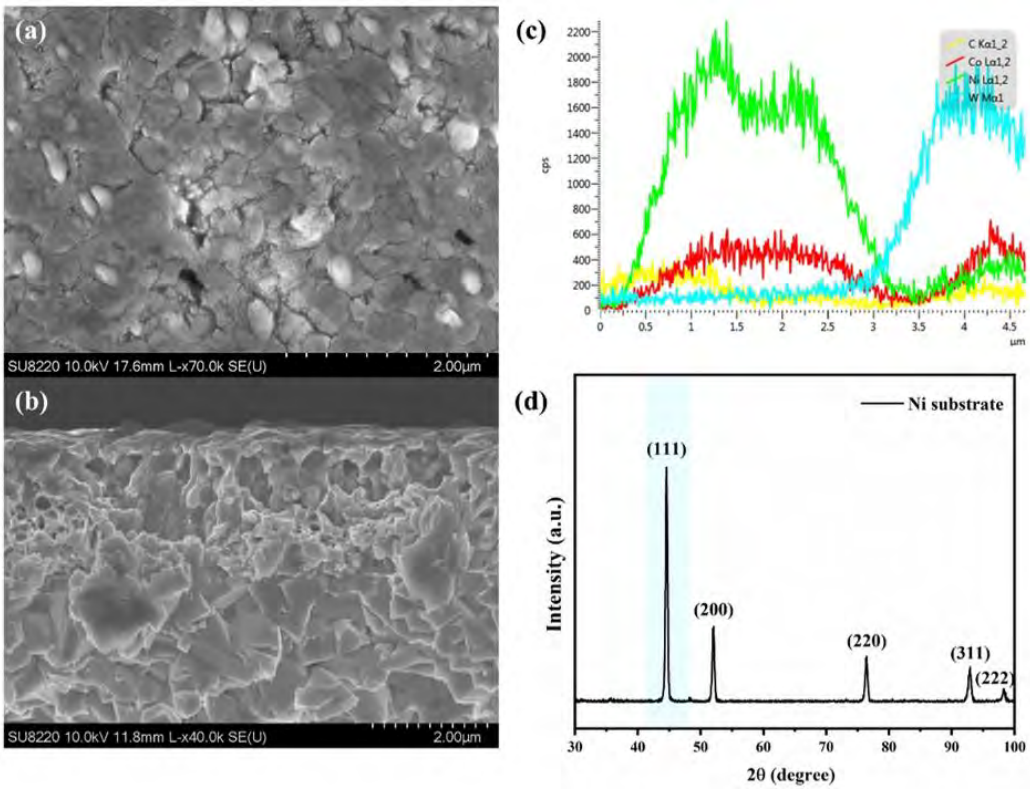

Fig. S1. Characterization of the Ni substrate: (a) Surface morphology, (b) Cross-section morphology, (c) Cross-sectional elemental distributions, and (d) XRD pattern.

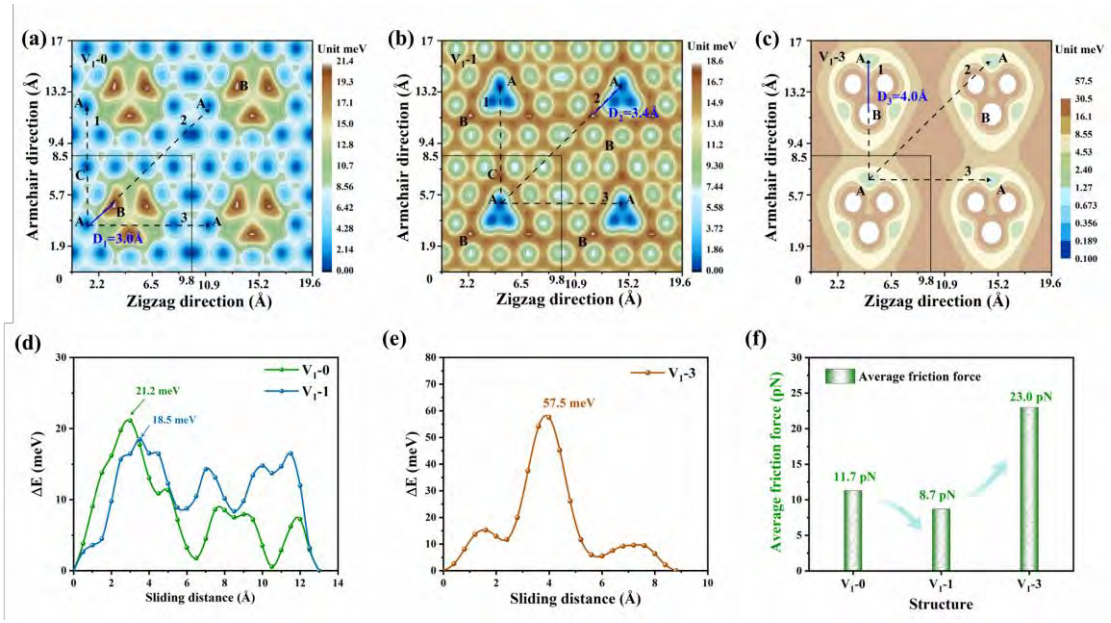

Fig. S2. Friction properties of V_1-0, V_1-1, and V_1-3 at 0 GPa contact stress: Potential energy surface of (a) V_1-0, (b) V_1-1 and (c) V_1-3 (The black number marked next to the dotted line refers to the path number); Maximum energy barrier along sliding paths for (d) V_1-0, V_1-1, and (e) V_1-3. (f) Calculated average friction force.

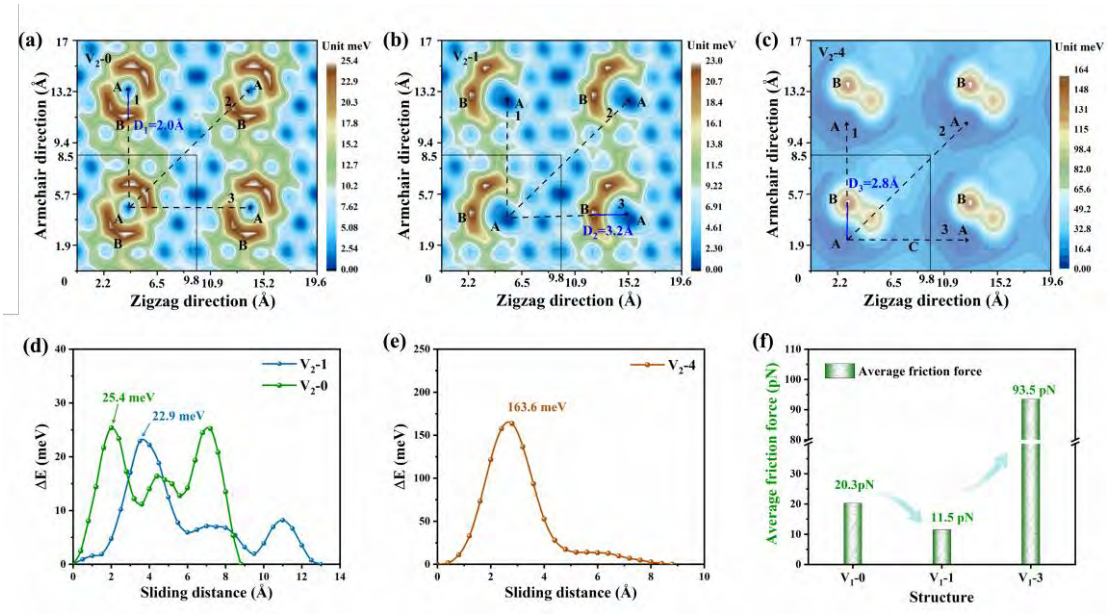

Fig. S3. Friction properties of V_2-0, V_2-1, and V_2-4 at 0 GPa contact stress: Potential energy surface of (a) V_2-0, (b) V_2-1 and (c) V_2-4 (The black number marked next to the dotted line refers to the path number); Maximum energy barrier along sliding paths for (d) V_2-0, V_2-1, and (e) V_2-4. (f) Calculated average friction force.

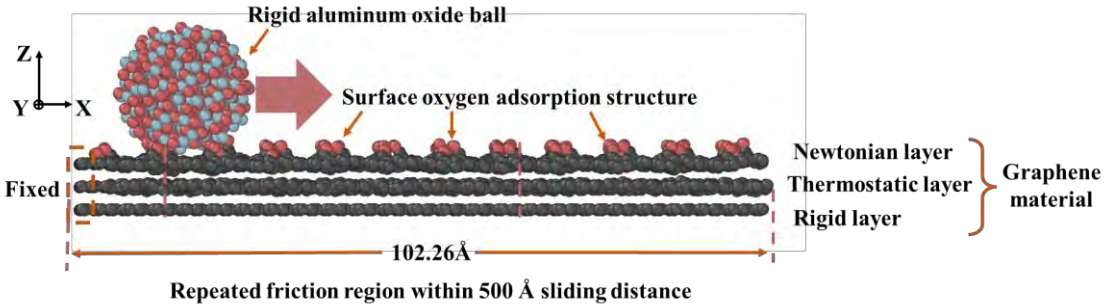

Fig. S4. The relaxed poly-oxygen structure models induced friction after the downward process. The grey, red, and blue spheres represent carbon, oxygen, and aluminum atoms respectively.

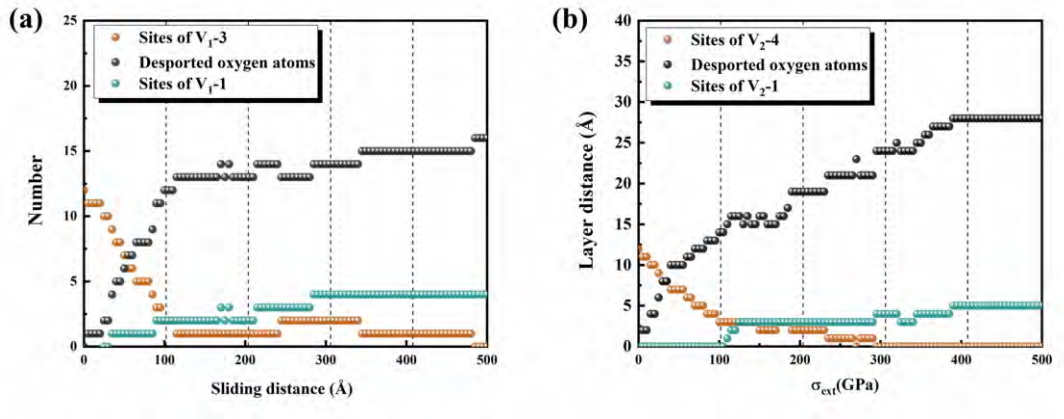

Fig. S5. Raw data of the variation of the number of poly-oxygen structures, desorpted oxygen atoms, and oligo-oxygen structures with the friction sliding distance of single vacancy structure (a) and double vacancy structure (b), respectively.

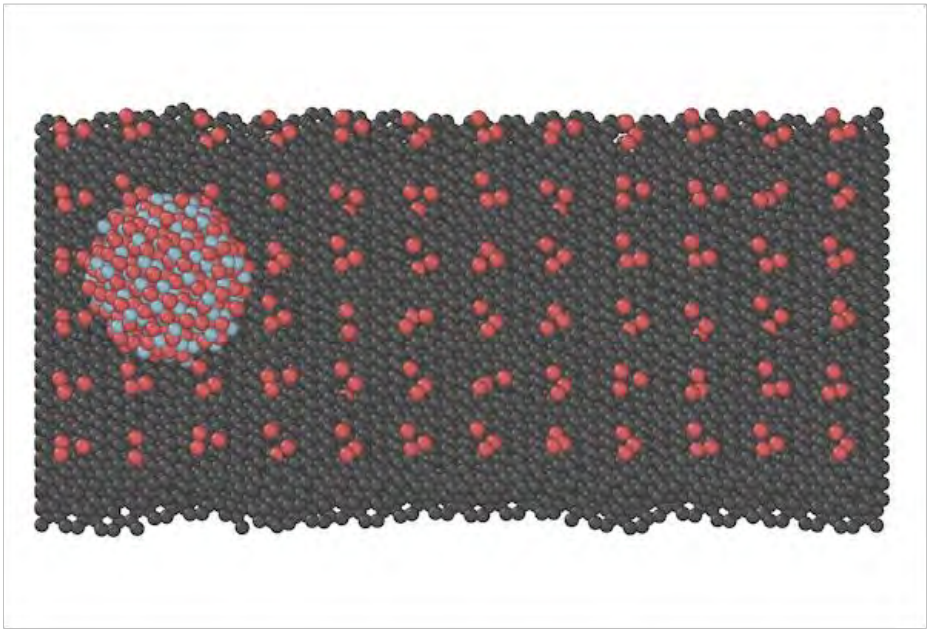

Fig. S6. Molecular dynamics simulation of the complete induced-friction process from poly-oxygen structures (V_1-3) to oligo-oxygen structures (V_1-1).

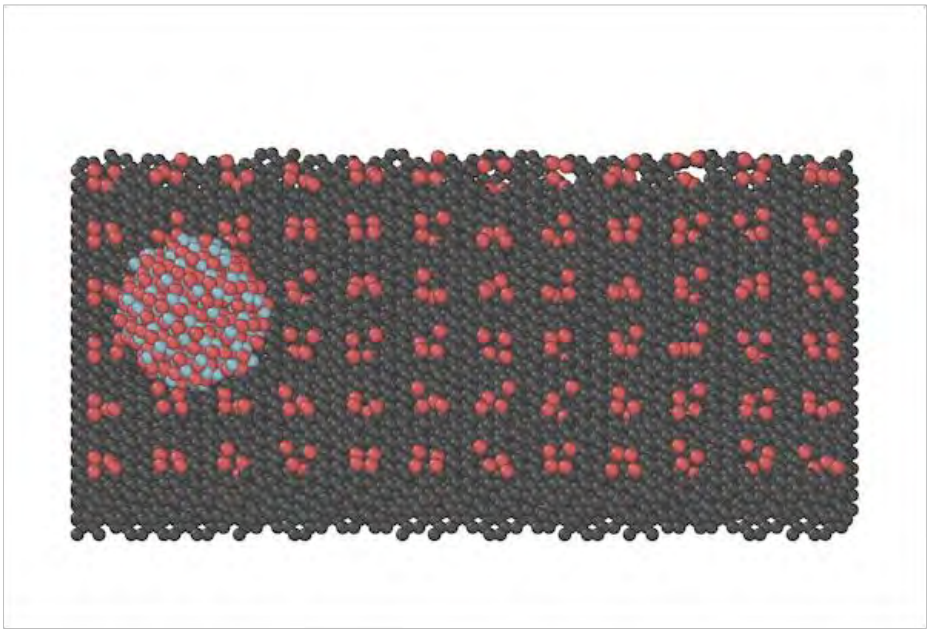

Fig. S7. Molecular dynamics simulation of the complete induced-friction process from poly-oxygen structures (V_2-4) to oligo-oxygen structures (V_2-1).

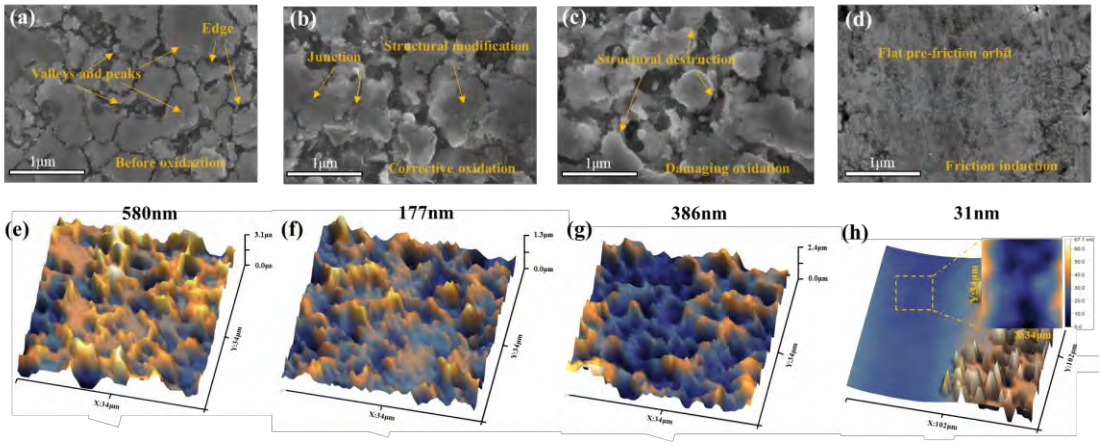

Fig. S8. Morphological, topographical, and structural characterization of the graphenic materials for different oxidation time or friction treatment: SEM surface morphologies of (a) GM-0, (b) GM-10, (c) GM-30, and (d) Induced GM -30; Three-dimensional morphological maps (34 μm × 34 μm) of (e) GM-0, (f) GM-10, (g) GM-30, and (h) Induced GM-30. The marked numbers are the value of surface roughness.

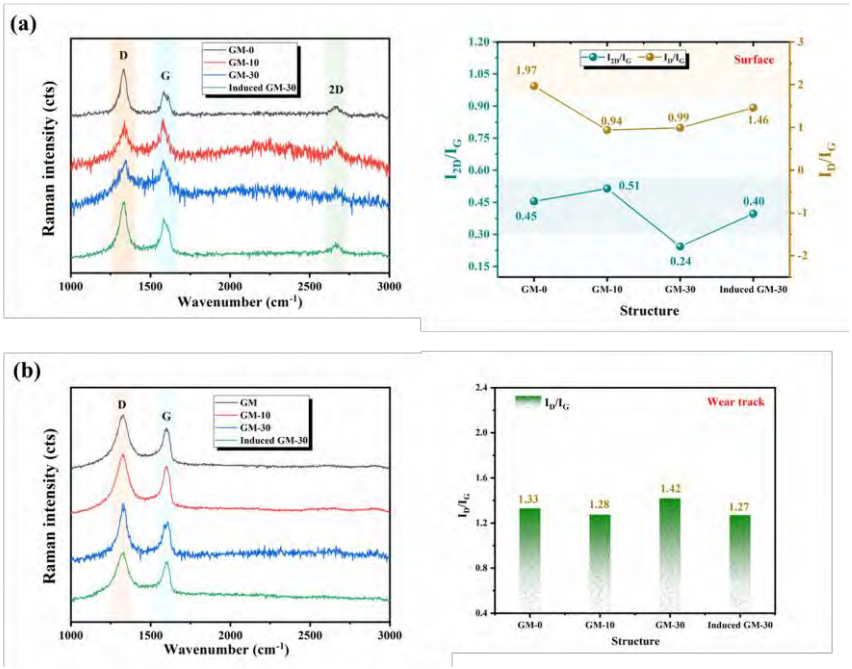

Fig. S9. (a) Raman scattering spectra and statistical distributions of I_D/I_G and I_{2D}/I_G ratios of the surface before friction; (b) Raman scattering spectra and the statistical distributions of I_D/I_G ratios of the edge of the wear tracks.

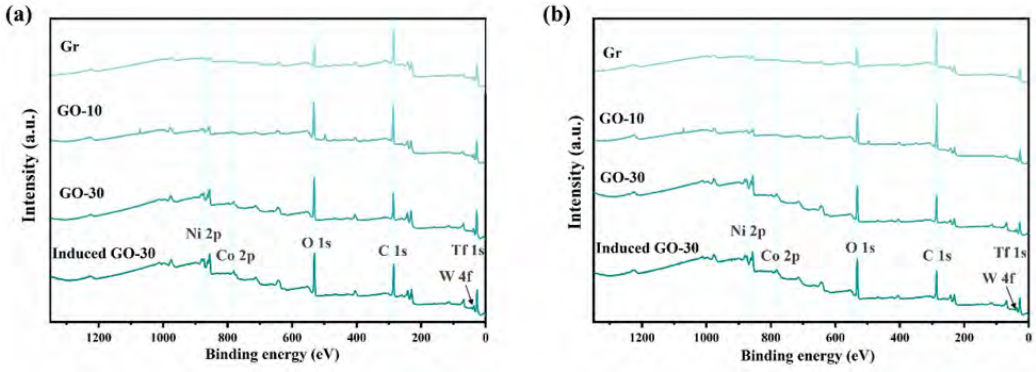

Fig. S10. (a) XPS survey spectra of the coating surface; (b) XPS survey spectra of the edge of the wear tracks.

Table S1. Structural binding energies (E) of V_1-0, V_1-1, V_1-3, V_2-0, V_2-1, and V_2-4 calculated by $E = \frac{E_{total} - N_i E_{iso}^i}{\sum N_i}$, where E_{total} is the total energy of the graphene system, E_{iso}^i is the energy of the isolated atom (i = Ni, Co, C), and Ni is the number of whole atoms. The binding energy of carbon-based materials is roughly 7.3 eV/atom. All the structures have good stability, as evidenced by the reasonable negative E.

Structure	E (eV/atom)
V_1-0	-7.480046076
V_1-1	-7.492665226
V_1-3	-7.407084135
V_2-0	-7.484744236
V_2-1	-7.483914678
V_2-4	-7.382147108

Table S2. Sample definitions and processing parameters.

Samples	Name	Parameters
Ni solid solution (2 μm depth)	Ni substrate	(1) PVD deposition: Pre-evacuation vacuum 0.0009 Pa, working air pressure 0.48 Pa, argon as an ion source, constant DC power 80 W sputtering nickel target, deposition time 144 min; (2) Annealing: Temperature of 700 ℃ for 60 min; cooling rate of 10 ℃/min.
Graphenic material	GM-0	(1) HFCVD deposition: 10 sccm CH_4, 1,000 sccm H_2, filament temperature of 2,000 ℃, working pressure of 1 mbar, and deposition time of 10 min; (2) Oxygen plasma treatment: Pre-evacuation vacuum 0.0009 Pa, working air pressure 0.48 Pa, oxygen as an ion source, varying treatment time of 0 min, 10 min, 30 min; (3) Induced friction: 0.1N load, 60 rpm for 2 min, ambient conditions (25℃, 50%RH).
Graphenic material with 10 min oxygen plasma treatment	GM-10	
Graphenic material with 30 min oxygen plasma treatment	GM-30	
Graphenic material with 30 min oxygen plasma treatment and 120 cycles induced friction	Induced GM-30	

Table S3. Fitting equations and correlation coefficients (R) of the lines in Fig. 2 for the layer distance and external stress (σ_{ext}) applied to V_1-0, V_1-1, V_1-3, V_2-0, V_2-1, and V_2-4.

Structures	Fitting equations	Correlation coefficients (R)
V_1-0	z= -0.0028σ_{ext}^3+0.0264σ_{ext}^2-0.1074σ_{ext}+3.269	0.998
V_1-1	z= -0.0028σ_{ext}^3+0.0252σ_{ext}^2-0.0999σ_{ext}+3.258	0.998
V_1-3	z= -0.0042σ_{ext}^3+0.0483σ_{ext}^2-0.3287σ_{ext}+4.6432	0.9999
V_2-0	z= -0.0032σ_{ext}^3+0.0279σ_{ext}^2-0.1072σ_{ext}+3.2652	0.9989
V_2-1	z= -0.0028σ_{ext}^3+0.0267σ_{ext}^2-0.1108σ_{ext}+3.2808	0.9988
V_2-4	z = 0.0044σ_{ext}^3-0.03σ_{ext}^2-0.1056σ_{ext}+4.0044	0.9992